AGU PUBLICATIONS

JGR

Journal of Geophysical Research: Solid Earth

RESEARCH ARTICLE

10.1002/2013JB010717

Key Points:
- The force balance in East Africa is dominated by lithospheric buoyancy forces
- Lithospheric weakening required to initiate rifting along most of East Africa

Supporting Information:
- Readme
- deviatoric stress compensated
- deviatoric stress uncompensated
- deviatoric stress eqm2008
- total deviatoric stress field compensated
- total deviatoric stress field uncompensated
- total deviatoric stress field eqm2008
- stress field boundary compensated
- stress field boundary uncompensated
- stress field boundary egm2008
- gpe compensated
- gpe eqm2008
- gpe uncompensated
- strain rate africa stamps
- gps data

Correspondence to:
D. S. Stamps,
dstamps@mit.edu

Citation:
Stamps, D. S., L. M. Flesch, E. Calais, and A. Ghosh (2014), Current kinematics and dynamics of Africa and the East African Rift System, *J. Geophys. Res. Solid Earth*, *119*, 5161–5186, doi:10.1002/2013JB010717.

Received 24 SEP 2013
Accepted 19 MAY 2014
Accepted article online 26 MAY 2014
Published online 16 JUN 2014

Current kinematics and dynamics of Africa and the East African Rift System

D. S. Stamps[1,2], L. M. Flesch[1], E. Calais[3], and A. Ghosh[4]

[1]Department of Earth, Atmospheric and Planetary Sciences, Purdue University, West Lafayette, Indiana, USA, [2]Now at Massachusetts Institute of Technology, [3]Department of Geosciences, UMR CNRS 8538, Ecole Normale Supérieure, Paris, France, [4]Centre for Earth Sciences, Indian Institute of Science, Bangalore, India

Abstract Although the East African Rift System (EARS) is an archetype continental rift, the forces driving its evolution remain debated. Some contend buoyancy forces arising from gravitational potential energy (GPE) gradients within the lithosphere drive rifting. Others argue for a major role of the diverging mantle flow associated with the African Superplume. Here we quantify the forces driving present-day continental rifting in East Africa by (1) solving the depth averaged 3-D force balance equations for 3-D deviatoric stress associated with GPE, (2) inverting for a stress field boundary condition that we interpret as originating from large-scale mantle tractions, (3) calculating dynamic velocities due to lithospheric buoyancy forces, lateral viscosity variations, and velocity boundary conditions, and (4) calculating dynamic velocities that result from the stress response of horizontal mantle tractions acting on a viscous lithosphere in Africa and surroundings. We find deviatoric stress associated with lithospheric GPE gradients are ~8–20 MPa in EARS, and the minimum deviatoric stress resulting from basal shear is ~1.6 MPa along the EARS. Our dynamic velocity calculations confirm that a force contribution from GPE gradients alone is sufficient to drive Nubia-Somalia divergence and that additional forcing from horizontal mantle tractions overestimates surface kinematics. Stresses from GPE gradients appear sufficient to sustain present-day rifting in East Africa; however, they are lower than the vertically integrated strength of the lithosphere along most of the EARS. This indicates additional processes are required to initiate rupture of continental lithosphere, but once it is initiated, lithospheric buoyancy forces are enough to maintain rifting.

1. Introduction

A fundamental component of the theory of plate tectonics not fully understood is the balance of forces required to initiate and sustain continental breakup. It is widely accepted that large-scale deformation of the lithosphere is controlled by a combination of (1) buoyancy forces that arise from lateral gradients in gravitational potential energy (GPE) within the crust and mantle-lithosphere [e.g., *Artushkov*, 1973; *Hager and O'Connell*, 1981; *Coblentz et al.*, 1994] and (2) boundary forces acting at the sides and base of lithospheric plates [e.g., *Forsyth and Uyeda*, 1975; *Richardson et al.*, 1979; *Kusznir and Park*, 1984; *Lithgow-Bertelloni and Guynn*, 2004; *Bird et al.*, 2008; *Forte et al.*, 2010; *Ghosh and Holt*, 2012]. The relative contribution of these forces is, however, difficult to determine. In addition, these contributions are likely to vary regionally and according to the tectonic context. This applies to continental rifting, a process where the role of buoyancy versus boundary forces remains debated [e.g., *Ruppel*, 1995].

We address this problem in the East African Rift System (EARS), the Earth's largest subaerial continental rift system. Its scale and diverse extensional settings make it a favorable natural laboratory to quantify the relative contribution of forces leading to sustained continental breakup. In addition, Africa is mostly surrounded by oceanic spreading centers, which provides a unique setting shielded from the influence of tractions from adjacent plates and pull from slabs. As a result, forces acting on the African lithosphere are derived solely from a combination of GPE gradients (which include epierogenic effects from vertical tractions) and viscous coupling with horizontal mantle flow at the base of the lithosphere. Some studies claim that the latter dominates the lithospheric stress budget in East Africa [e.g., *Steinberger et al.*, 2001; *Quéré and Forte*, 2006; *Bird et al.*, 2008; *Ghosh and Holt*, 2012], while others argue that forces arising from GPE gradients within the lithosphere dominate [e.g., *Coblentz and Sandiford*, 1994; *Stamps et al.*, 2010; *Craig et al.*, 2011; *Moucha and Forte*, 2011]. At the global scale, *Ghosh et al.* [2008] and *Ghosh and Holt* [2012] argue from dynamic models that 50 to 70% of the deviatoric stress field in the lithosphere results from viscous coupling with mantle flow.

Here we investigate this issue by first quantifying the vertically averaged deviatoric stress field from gradients in lithospheric GPE acting on the African lithosphere taking the thin-sheet approximation [e.g., *Bird and Piper*, 1980; *England and McKenzie*, 1982] and solving the depth-averaged 3-D force balance equations for 3-D deviatoric stress following *Flesch et al.* [2001, 2007]. Second, we invert for a stress field boundary condition required to best fit the style of the observed surface deformation obtained from our new kinematic model. We assume this stress field boundary condition represents horizontal tractions from mantle flow because Africa is not strongly influenced by subduction-related forces. The inversion for the stress field boundary condition results in the minimum stress due to horizontal mantle tractions. Mantle upwellings beneath the EARS may induce stresses at the base of the lithosphere with similar orientations as deviatoric stress from GPE gradients; thus, horizontal mantle tractions may be larger than our estimate. Therefore, in a third step we compute a dynamic velocity field driven by velocity boundary conditions derived from our new kinematic model, body forces, and lateral variations in effective viscosity. We then compute a dynamic velocity field that includes force contributions from the mantle flow field of *Ghosh and Holt* [2012]. Here we find that velocities driven by GPE gradients alone produce the correct direction and rate of opening across the EARS with a weighted root mean square (WRMS) value of 2.8 mm/yr. The addition of dynamic velocities from horizontal mantle tractions over predicts surface kinematics by at least twice the rate of GPS observations. This work benefits from an updated kinematic data set constraining surface motions and deformation within the EARS, including the incorporation of microplates [*Hartnady*, 2002; *Calais et al.*, 2006; *Horner-Johnson et al.*, 2007; *Stamps et al.*, 2008; *DeMets et al.*, 2010; *Saria et al.*, 2013]. Our results indicate that horizontal basal tractions are not required to drive the opening of the EARS and gradients in GPE dominate the force balance in East Africa.

2. Kinematics

2.1. Methodology

To constrain surface kinematics needed to evaluate the dynamics of Africa and the East African Rift System we compute a continuous strain rate and velocity field using geodetically derived plate angular velocities, GPS velocities (Figures 1a and 1b), earthquakes from the National Earthquake Information Center (NEIC) catalog, and earthquake moment tensors from the Global Centroid Moment Tensor catalog (Figures 1c and 1d) [*Dziewonski et al.* 1981, 1996, and references therein]. We first assign a low-base-level isotropic variance to all regions to reflect plate rigidity following *Haines and Holt* [1993], *Holt and Haines* [1995], and *Haines et al.* [1998]. We define the base-level variance as 0.0088 (equivalent to 0.6 mm/yr) to be consistent with the most recent geodetic solution for a rigid Nubian plate [*Saria et al.*, 2013]. We then use the Kostrov summation [*Kostrov*, 1974] to sum the seismic moment in each grid area where focal mechanisms provide an a priori estimate of the observed strain. Simultaneously, we apply associated anisotropic variances in areas with focal mechanism data (see *Haines et al.*, 1998, for details). In regions with seismicity, but no focal mechanism data, we increase isotropic variances by a factor of 20 [*Finzel et al.*, 2011] to allow strain to preferentially accommodate within these areas. Following *Haines et al.* [1998], we use bicubic Bessel splines to jointly fit GPS velocities and strain rates obtained from the summed earthquake moment tensors at a $1^\circ \times 1^\circ$ resolution.

Seismicity in the East African Rift System is characterized by low-magnitude, <50 km deep crustal earthquakes with rare events greater than *M*6 and deeper than 50 km [i.e., *Lindenfield and Rümpker*, 2011]. Although larger earthquakes reflect large-scale tectonic motions more accurately than smaller ones, they would also largely dominate the strain rate solution [*Kreemer et al.*, 2000]. This would bias the interpretation in the case of an incomplete catalog, as is the case for the EARS, resulting in an inaccurate depiction of regional deformation patterns. *Amelung and King* [1997] showed that strain released by smaller earthquakes averaged over broad regions effectively portrays large-scale patterns of deformation. We therefore used <*M*6 earthquakes for strain rate calculations in the EARS. Our model region includes a subduction zone of limited lateral extent associated with the Nubia-Eurasia and Arabia-Eurasia convergent zones. Since we are modeling only surface deformation, we use earthquakes shallower than 50 km in these regions.

Since the earthquake record spans a fraction of the geologic record, we calculate uncertainties for earthquake data larger than the GPS data. This allows the interpolation to preferentially fit the magnitudes of the GPS because the uncertainties are smaller than the earthquakes. We retain the earthquake data in our calculation because it provides important constraints on strain rate style and localization. Using kinematic models derived from present-day and geologic observations [*Stamps et al.*, 2008; *DeMets et al.*, 2010] or

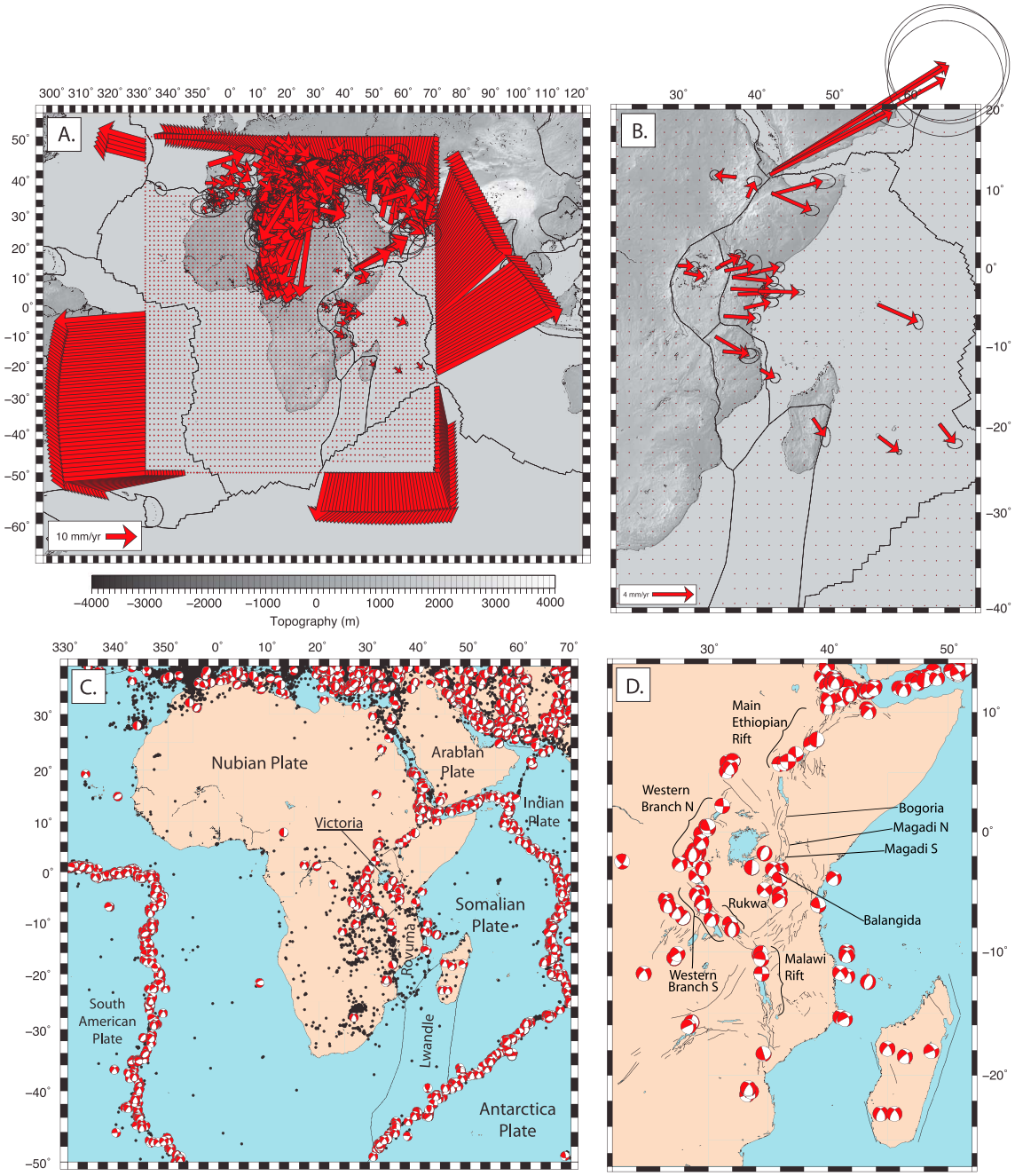

Figure 1. Overall tectonic setting and data sets used. (a and b) Red vectors show GPS velocities in a Nubia-fixed reference frame [*Vernant et al.*, 2004; *Reilinger et al.*, 2006; *Serpelloni et al.*, 2007; *Kogan et al.*, 2012; *Saria et al.*, 2013] within the interior of the region and velocity boundary constraints based on MORVEL [*DeMets et al.*, 2010]. Dots indicate locations of predicted velocities from kinematic models where GPS data are unavailable, and the background topography is from ETOPO5 (National Geophysical Data Center). All error ellipses are 95%. (c and d) Earthquake focal mechanisms from the Global Centroid Moment Tensor database with hypocenters above 50 km depth and magnitude less than 6. Black dots represent additional earthquakes from the NEIC catalog used in this work to define deforming regions. Traces of major faults along the EAR and rift segments are indicated in Figure 1d.

geodetic observations alone [*Saria et al.*, 2013], we calculate a pseudo-GPS velocity field of current plate motions every 1.5° within the interior of the Nubian, Somalian, North American, South American, Antarctica, Indian, Australian plates, and smaller plates such as Lwandle, Rovuma, and Victoria with imposed uncertainties of 0.6 mm/yr at each grid node up to ~75 km from plate boundaries. At each of the 384 nodes along the grid boundary, we assign velocities using the Mid-Ocean Ridge VELocity (MORVEL) model of plate motions [*DeMets et al.*, 2010]. To accommodate strain across the mid-oceanic ridges along the boundary of our grid,

we amplify the uncertainties to 20 mm/yr such that bicubic Bessel spline interpolation can fit focal mechanism styles and the surrounding velocities as needed. We also include GPS velocities within and around the EARS, on the Somalian plate, and in Eurasia obtained from *Vernant et al.* [2004], *Reilinger et al.* [2006], *Serpelloni et al.* [2007], *Kogan et al.* [2012], and *Saria et al.* [2013] (Figures 1a and 1b, red vectors). All geodetic observations are transformed into a Nubia-fixed reference frame through a Helmert transformation based on GPS sites common to all studies (GOUG, HARB, HRAO, MAS1, NKLG, PHLW, SUTH, TGCV, and YKRO). We require that campaign GPS measurements span at least 6 years of observations, continuous GPS data have at least 2.5 years of observations, and uncertainties of the observations are no more than 20% of the velocity magnitude. The continuous site on Madagascar (ABPO), which is the only continuous GPS observation constraining the Lwandle plate, has an uncertainty of 25% of its velocity magnitude. We add this observation into our input since it constraints the Lwandle plate. We also impose a rigid Nubia plate within 0.6 mm/yr as defined by *Saria et al.* [2013] and do not include Nubia plate GPS velocities in our input.

2.2. Results

The continuous strain rate field we calculate here (Figures 2a and 2b) is consistent with the broad-scale tectonic features of the study area. Across oceanic spreading ridges and the EARS strain rates are mostly extensional, and they are mostly compressional across the Arabia-Nubia-Eurasia collisional zone. As expected because of the model input, strain rates within continental interiors and oceanic basins are low, while higher strain rates are localized along plate boundaries.

Within the EARS, strain is extensional overall with the exception of a small compressional region (~0.5×10^{-8}/yr) to the SE of southern Africa, south of the proposed triple junction of the Rovuma, Lwandle, and Nubian plates. Strain rates range from 0.01 to 1×10^{-8}/yr, and directions vary along the rift. In the Main Ethiopian Rift, strain rate tensors are orientated WNW-ESE and rotate to a NW-SE direction further north. In the central EARS, larger strain rates localize along the Eastern and Western branches. Strain rates across the central EARS are principally extensional, consistent with the pure normal-faulting focal mechanism calculated by *Delvaux and Barth* [2010].

Predicted velocities from the strain rate model are within GPS uncertainties at locations where we have data (Figures 2c and 2d) with a WRMS = 0.7 mm/yr. We also fit both pseudo-velocities and GPS data combined with a WRMS = 0.3 mm/yr indicating the spline interpolation appropriately fits input observations.

A comparison with the Global Strain Rate Map (GSRM) [*Kreemer et al.*, 2003], which also uses the methodology of *Haines et al.* [1998], shows good agreement overall. Because GSRM is global and predates many of the GPS observations presently available, its resolution in Africa is limited. As a result, while both strain rate fields show E-W tensional strain across the EARS, the one calculated here has higher spatial variability. GSRM also does not include the Victoria, Rovuma, and Lwandle microplates and therefore shows mostly diffuse, uniform tensional strain across the EARS, while our model shows localized tensional strain in narrow rift zones, where we allowed strain to concentrate.

3. Lithospheric Deviatoric Stress

3.1. Methodology

The strain rate field we present here is based on updated GPS data, earthquake information, and newly resolved microplates between the Nubian and Somalian plates. It provides spatially variable kinematic constraints along the EARS that were not available for previous and global geodynamic studies of Africa [*Ghosh et al.*, 2008, 2009; *Ghosh and Holt*, 2012]. Gradients in basal shear stress and GPE (which include epierogenic effects) drive the surface strain rate field, and we separate contributions from each source by first quantifying the deviatoric stress field associated with GPE variations and then solving a stress field boundary condition associated with stresses produced on the base and sides of our region to determine a total deviatoric stress field for Africa. Solving for each source of stress independently is an advantage of this method.

We first solve the depth averaged 3-D force balance equations for 3-D deviatoric stress following *Flesch et al.* [2001, 2007] written in Einstein notation:

$$\frac{\partial}{\partial x_\beta}\left(\overline{\tau}_{\alpha\beta} + \delta_{\alpha\beta}\overline{\tau}_{\gamma\gamma}\right) + f_{1\alpha} + f_{2\alpha} = 0 \quad (1)$$

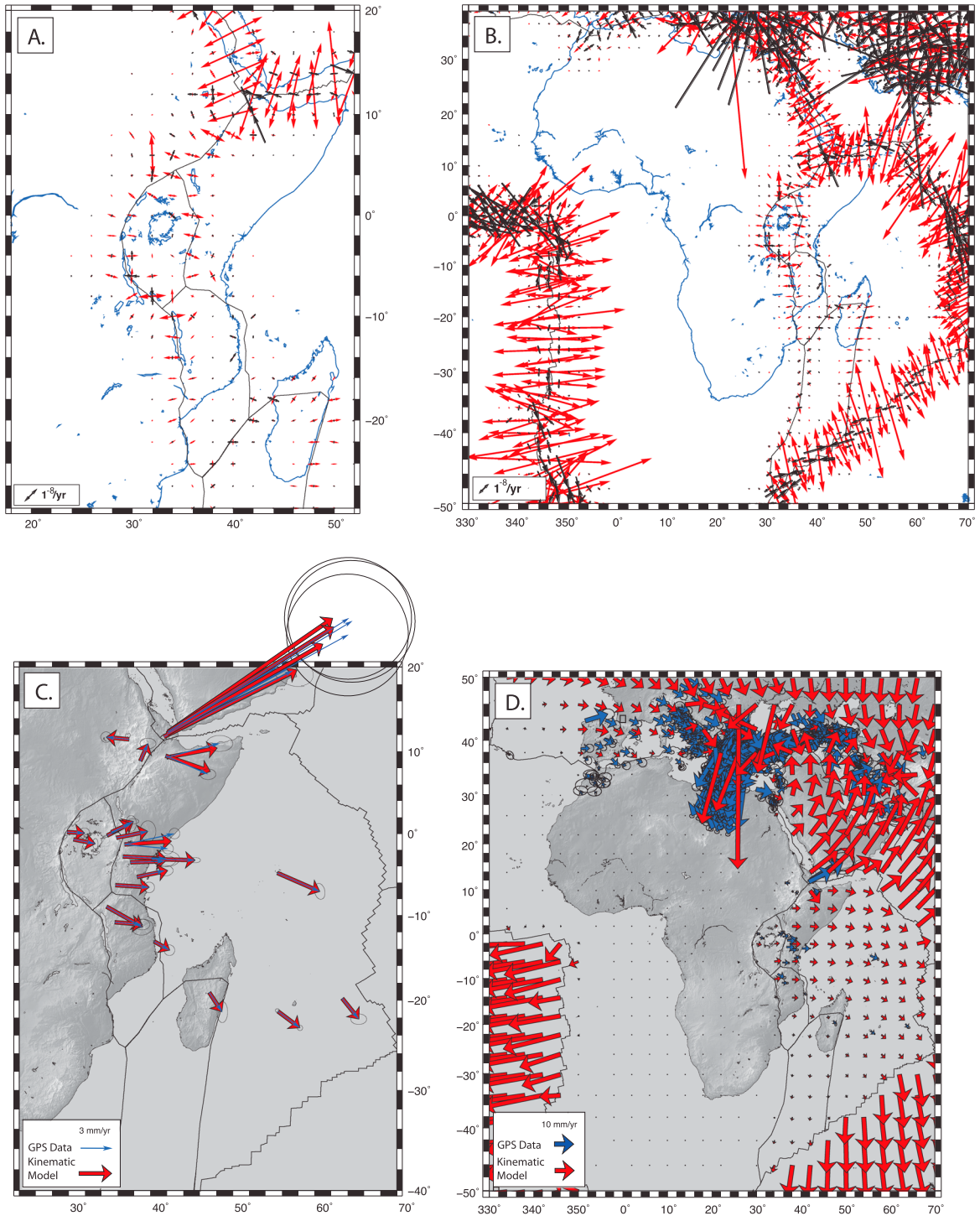

Figure 2. (a and b) Continuous strain rate field. Principal tensor components shown in red are extensional and in black are compressional. (c and d) Continuous velocity field with GPS data represented as blue vectors and red vectors as kinematic velocities with topography in the background from ETOPO5 (National Geophysical Data Center).

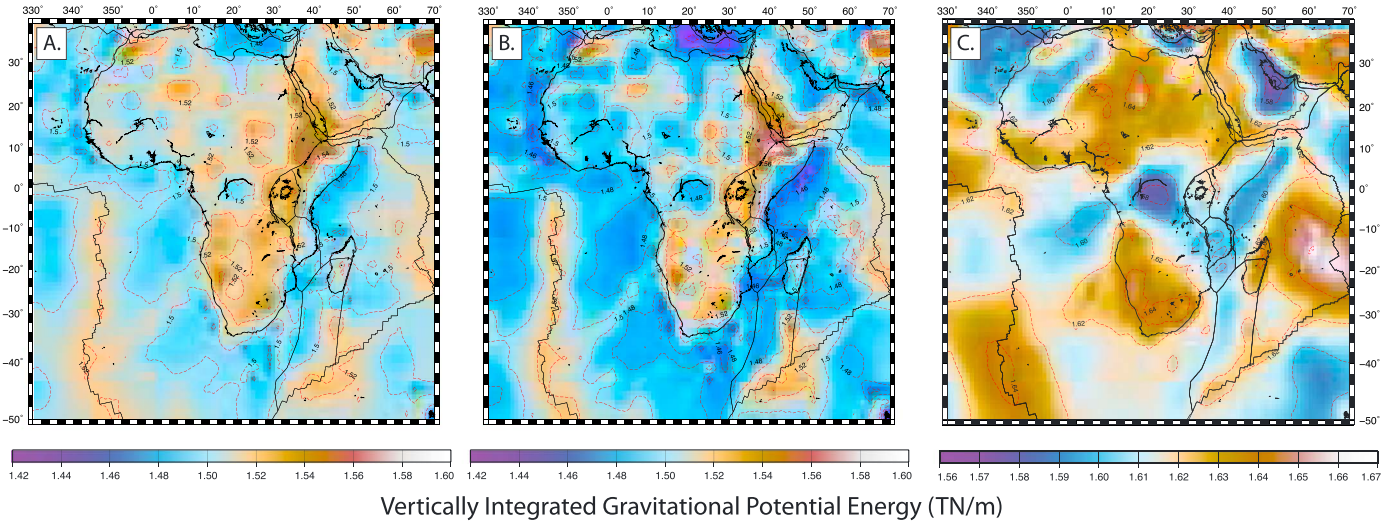

Figure 3. (a) Vertically averaged vertical stress (GPE) for a lithosphere constrained by ETOPO5 and CRUST2.0 crustal density variations and thicknesses [*Bassin et al.*, 2000]. This lithospheric model is compensated by lateral variations in density from the Moho to a depth of 100 km. (b) Same as Figure 3a but for an uncompensated lithosphere with uniform density of 3300 $\frac{\text{kg}}{\text{m}^3}$ from the base of the Moho to 100 km depth. (c) Vertically averaged vertical stress for a 100 km thick lithosphere constrained by EGM2008 geoid undulations with up to order and degree 7 removed.

where $\overline{\tau}_{\alpha\beta}$ represents vertically averaged deviatoric stress, $\delta_{\alpha\beta}$ is the Kronecker delta, $\overline{\tau}_{\gamma\gamma} = \overline{\tau}_{xx} + \overline{\tau}_{yy} = -\overline{\tau}_{zz}$, $f_{1\alpha} = \frac{\partial\overline{\sigma}_{zz}}{\partial x_\alpha}$ (body force, where $\overline{\sigma}_{zz}$ is the vertically averaged vertical stress we term GPE), and $f_{2\alpha} = \frac{1}{L}\overline{\tau}_{x_\alpha z}$ which represents the vertical integrals of horizontal tractions acting at the base of the lithosphere.

We estimate $\overline{\sigma}_{zz}$ in two ways. First, estimates are based on CRUST2.0 [*Bassin et al.*, 2000], and we define the vertically averaged vertical stress:

$$\overline{\sigma}_{zz} = -\frac{1}{L}\int_0^h \left(\int_0^z \rho(z')g\mathrm{d}z'\right)\mathrm{d}z \tag{2}$$

where h is the thickness of the lithosphere, z is depth, g is gravitational acceleration, ρ is density, and L is the depth of compensation (100 km). We use ETOPO5 topography and depth-dependent crustal densities from the CRUST2.0 model to define the lithospheric density distribution and constrain mantle-lithosphere density beneath the Moho down to a depth of 100 km either by assuming a uniform density of 3300 kg·m^{-3} (an uncompensated case) or calculating lateral density variations to achieve isostatic compensation with respect to an average mid-oceanic ridge density of 3195 kg m^{-3} (Figures 3a and 3b). The density compensation assumes that pressure is constant at a depth of 100 km and thus the dynamic topography contribution is zero but provides a way to account for upper mantle anomalies that may arise from, for example, compositionally distinct cratonic roots [*Ritsema et al.*, 1998; *King*, 2005; *Lee et al.*, 2011] or thermal anomalies associated with asthenospheric upwellings. Beneath the Ethiopian and East African plateaux and along the Red Sea our calculation of laterally varying mantle-lithosphere density results in a negative (i.e., buoyant) density anomaly that correlates with seismic tomography studies that observe slow seismic shear wave anomalies [e.g., *Green et al.*, 1991; *Davis and Slack*, 2002; *Bastow et al.*, 2005; *Nyblade*, 2011; *Adams et al.*, 2012]. The former assumption of a uniform mantle density also assumes that the lithosphere is not in isostatic balance, and topography is partly supported by radial tractions; thus, it implicitly includes the effect of dynamic topography.

Second, for comparison, and to assess the uncertainties in GPE estimates, we also compute an estimate of vertically averaged vertical stress from the EGM2008 geoid undulations (Figure 3c) assuming geoid anomalies relate to density variations in isostatically compensated areas following *Coblentz et al.* [1994, and references therein]:

$$\overline{\sigma}_{zz} = \frac{U_l}{L} = U_r - \Delta N\left(\frac{g^2}{2\pi G}\right) \tag{3}$$

where ΔN is the geoid anomaly from EGM2008, U_r is a reference potential energy for a lithospheric column at the mid-oceanic ridges, g is gravitational acceleration, and G is the gravitational constant. U_l is vertically

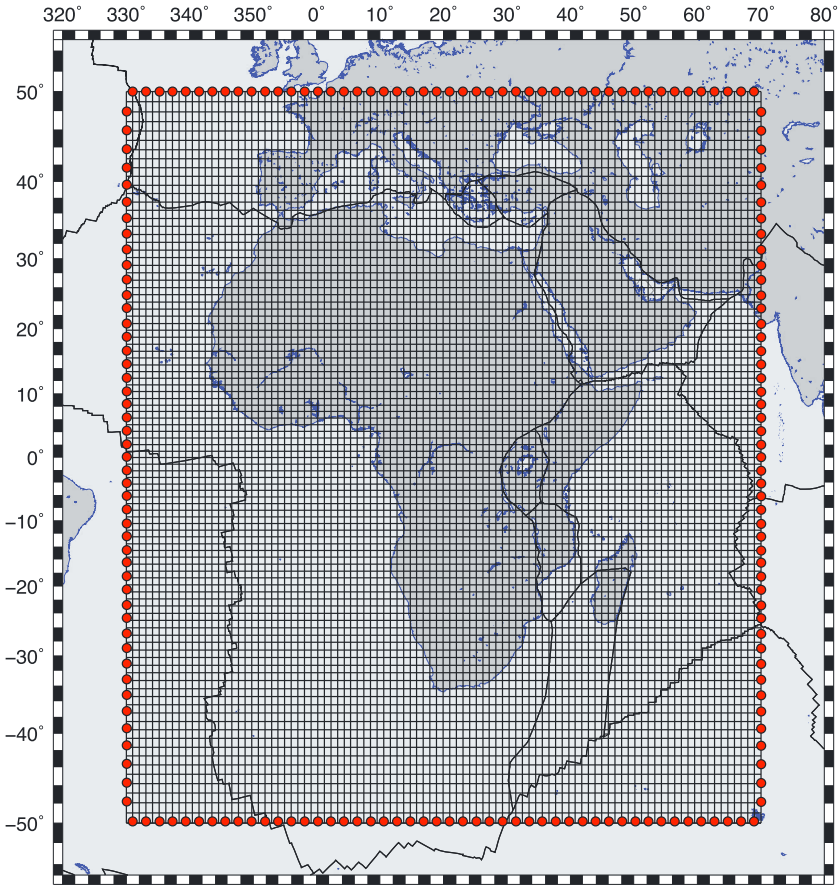

Figure 4. Grid used for all models. Red circles show locations of 96 nodes at every 2° along the model boundary.

averaged over the thickness of the lithosphere. Geoid heights result from density variations in both the lithosphere and mantle [i.e., *Sleep*, 1990]. To approximately isolate geoid undulations associated with the lithosphere, we filter spherical harmonics up through order and degree 7 such that effects from the deeper mantle buoyancies are removed.

To solve equation (1) we reduce the number of unknowns by imposing that the solution be a minimum such that with an estimate of GPE ($f_{1\alpha}$) everywhere within our uniform grid of 0.5° × 0.5° (Figure 4) we can directly solve equation (1) to determine the minimum vertically averaged deviatoric stress without the need for rheologic estimates a priori [e.g., *Flesch et al.*, 2000, 2001]. Previous work has shown the minimum solution produces the same magnitudes as a solution that does not assume minimum energy [*Flesch et al.*, 2001], which suggests the minimum assumption is robust. We also demonstrate that this holds for Africa in section 4 below.

Vertically averaged deviatoric stress that we generate from GPE gradients using the compensated and uncompensated CRUST2.0 models and EGM2008 geoid undulations (Figures 5a–5c) show similar magnitudes (~5–20 MPa), with E-W tension across most of the EARS, tension in elevated southern Africa, and compression in the oceanic basins and the Congo Basin. The models using CRUST2.0 show tensional deviatoric stress across mid-ocean ridges, whereas the model that uses EGM2008 shows more variability. Additional differences in the models of vertically averaged deviatoric stress derived from CRUST2.0 and the model of vertically averaged deviatoric stress derived from EGM2008 geoid undulations are evident in western and northern Africa. These are areas that are the least constrained in CRUST2.0 because of the lack of regional seismic profiles. Crustal densities and thicknesses in these regions are based on geologic profiles determined from similar geologic provinces on Earth [*Bassin et al.*, 2000]. All three models compare qualitatively well in both magnitude and tensor style with the *Coblentz and Sandiford* [1994] geoid-based model

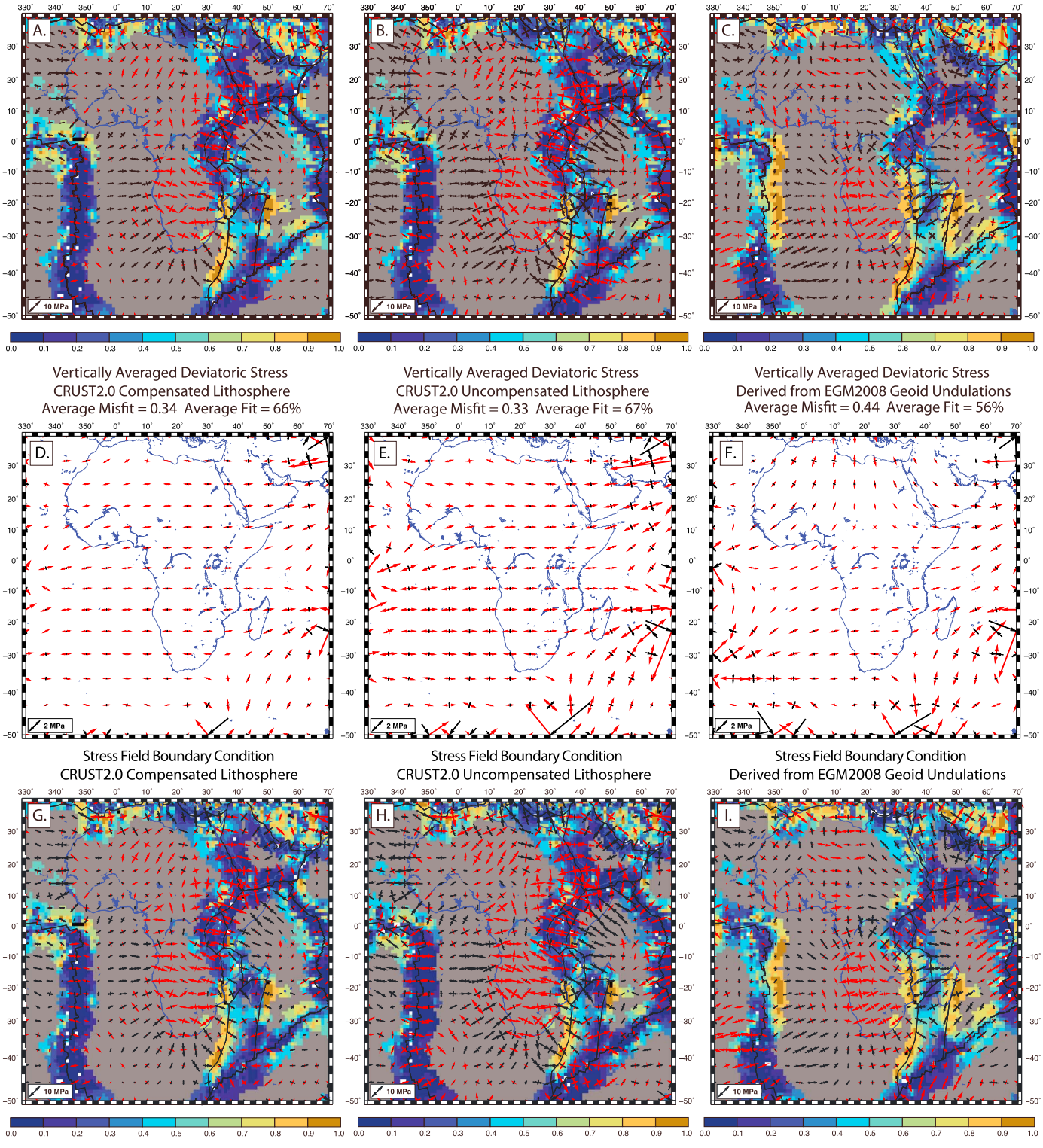

Figure 5

of deviatoric stress in Africa, the *Lithgow-Bertelloni and Guynn* [2004] deviatoric stress field derived from CRUST2.0, and the *Ghosh et al.* [2009] deviatoric stress field based on CRUST2.0.

We quantify one source of deviatoric stress arising from gradients in GPE and now investigate the role of horizontal mantle tractions, the other major force acting on the African plate. We follow the methodology presented in *Flesch et al.* [2007] to solve for a long-wavelength stress field boundary condition associated with either relative plate motion or tractions acting at the base of the lithosphere. Because Africa is surrounded mostly by spreading ridges, no side boundary force should be generated. Therefore, we assume that the stress field boundary condition represents the contribution of deviatoric stress driven by the coupling of the lithosphere with horizontal mantle tractions. To solve for the stress field boundary condition we first calculate three orthonormal basis functions at 96 nodes along the boundary of our grid using equation (1) with $f_{1\alpha}$ and $f_{2\alpha} = 0$. These 96 nodes are equivalent to three orthonormal basis functions every 2° (288 basis functions) and are defined by rotations w = (1, 0, 0), (0, 1, 0), and (0, 0, 1). Between each node are boundary segments for which we calculate the basis functions within the grid interior that corresponds to w, which are weighted by scaling factors determined in the inversion. The resulting long-wavelength stress field boundary condition is the linear sum of the stress responses and is added to vertically averaged deviatoric stress from GPE gradients to define the total vertically averaged deviatoric stress field:

$$\overline{\tau} = \overline{\tau}_o + \sum_{j=1}^{\text{nseg}} \sum_{i=1}^{3} a_{ij} \tau_{ij} \tag{4}$$

where $\overline{\tau}$ is the vertically averaged total deviatoric stress, $\overline{\tau}_o$ is the vertically averaged deviatoric stress associated with GPE variations, τ_{ij} are the basis functions, and a_{ij} are the scaling factors for the basis functions. We determine the scaling factors using an iterative least squares inversion such that the style of the vertically averaged total deviatoric stress tensor produces the best fit to the style of stress field indicators. To invert for the stress field boundary condition, we assume the lithosphere is isotropic, i.e., deviatoric stress and strain rate are collinear, use the style of strain rates as stress field indicators, and minimize [*Flesch et al.*, 2007]:

$$\sum_{\text{area } S} \left(T - \frac{\dot{\varepsilon} \cdot \overline{\tau}}{\dot{E}} \right) \triangle S \tag{5}$$

where

$$\dot{\varepsilon} \cdot \overline{\tau} = 2\overline{\tau}_{xx}\dot{\varepsilon}_{xx} + \overline{\tau}_{xx}\dot{\varepsilon}_{yy} + \overline{\tau}_{yy}\dot{\varepsilon}_{xx} + 2\overline{\tau}_{yy}\dot{\varepsilon}_{yy} + 2\overline{\tau}_{xy}\dot{\varepsilon}_{xy}$$

$$T = \left(2\overline{\tau}_{xx}^2 + 2\overline{\tau}_{xx}\overline{\tau}_{yy} + 2\overline{\tau}_{yy}^2 + 2\overline{\tau}_{xy}^2 \right)^{\frac{1}{2}}$$

$$\dot{E} = \left(2\dot{\varepsilon}_{xx}^2 + 2\dot{\varepsilon}_{xx}\dot{\varepsilon}_{yy} + 2\dot{\varepsilon}_{yy}^2 + 2\dot{\varepsilon}_{xy}^2 \right)^{\frac{1}{2}}$$

$\triangle S$ represents each grid area, $\dot{\varepsilon} \cdot \overline{\tau}$ is the dot product of the total vertically averaged deviatoric stress tensor and strain rate tensor, T is the second invariant of total vertically averaged deviatoric stress, and $\dot{E}$ is the second invariant of strain rate. Equation (5) is minimized when the principal deviatoric stress axis aligns with the principal strain rate axis so that the style and direction of each tensor matches. The assumption of collinear stress and strain rate tensors is a reasonable first-order approximation for Africa because well-developed

Figure 5. (a) Vertically averaged deviatoric stress tensors [*Stamps et al.*, 2010] for an isostatically compensated lithosphere constrained by CRUST2.0 [*Bassin et al.*, 2000] with the misfit plotted in the background. Gray regions indicate strain rate magnitudes are below the resolution of observations. (b) Same as Figure 5a but for an uncompensated lithosphere. (c) Same as Figures 5a and 5b but for a lithosphere constrained by EGM2008 geoid undulations. Differences in these models arise largely in areas where CRUST2.0 is the least constrained because there are no seismic profiles available. See text for further details. (d) Stress field boundary condition for a compensated lithosphere constrained by CRUST2.0. (e) Same as Figure 5d but for an uncompensated lithosphere. (f) Same as Figures 5d and 5e but for a model derived from EGM2008 geoid undulations. (g) Total vertically averaged deviatoric stress tensors for an isostatically compensated lithosphere constrained by CRUST2.0 with the misfit plotted in the background. (h) Same as Figure 5g but for an uncompensated lithosphere. (i) Same as Figures 5g and 5h but for a lithosphere constrained by EGM2008 geoid undulations.

Table 1. Misfit Statistics for Models of Lithospheric Stress and Qualitative Comparison for Observations of Compression in the Congo Basin (CB)

Model	Misfit	CB compression
GPE compensated	0.34	yes
Total compensated	0.31	yes
GPE uncompensated	0.33	yes
Total uncompensated	0.30	yes
EGM08	0.44	yes
Total EGM08	0.40	yes
GPE compensated + stress field boundary condition ×2	0.20	no
GPE compensated + stress field boundary condition ×10	0.29	no
GPE compensated + stress field boundary condition ×100	0.31	no
GPE compensated + stress from tractions	0.27	no

transform faults, where the direction of principal stress is anisotropic to the direction of strain rate, play a minor role in the tectonic setting. The major fault zones are dominated by normal faulting where maximum principal stress directions are typically collinear with deformation indicators as shown by *Delvaux and Barth* [2010].

The resolution of the method applied here is determined by the number of nodes along the boundary of the region. We compared models with 38 nodes and 96 nodes along the boundary of the gridded area. Doubling the number of degrees of freedom by increasing the number of nodes to 96 results in stress field boundary conditions that are 99.7% identical in style and vary by ~6% in magnitude with the differences focused at the edges of our grid. We choose the stress field boundary conditions derived from basis functions calculated every 2° because it provides a higher-resolution mathematical fit to the observed strain rate field.

3.2. Results

The resulting stress field boundary condition for both the compensated and uncompensated models are similar in both pattern and magnitude. Deviatoric stresses are E-W tensional across Africa with magnitudes on the order of 1–2 MPa overall and less than 1.6 MPa across the EARS (Figures 5d and 5e). The stress field boundary condition calculated for the EGM2008-derived model of vertically averaged deviatoric stress (Figure 5f) is comparable in both pattern and magnitude with exceptions in the northern half of the African continent. The differences in these models is due to the differences in their associated GPE.

The total vertically averaged deviatoric stress fields (Figures 5g–5i) show patterns very similar to the corresponding vertically averaged deviatoric stress fields from GPE gradients or EGM2008 geoid undulations but with slightly larger magnitudes (by ~1–2 MPa) because of the added stress field boundary conditions. Deviatoric stress magnitudes decrease by ~1–2 MPa in regions of subaerial compression for all models; however, we still resolve deviatoric compression in the Congo Basin, parts of western and northern Africa, and the oceanic basins. Regions of high topography exhibit deviatoric tension, such as the mid-oceanic ridges, the Zagros, Atlas, Alps, Carpathian, Hoggar, and Tibesti mountains, as well as the South African, East African, and Ethiopian plateaus and Madagascar. The additional stress contribution from basal tractions is within the 13% uncertainty in this method applied to Africa and surroundings, which we determine using a Monte Carlo approach. We calculate 100 randomized distributions of a 20% uncertainty on the maximum and minimum compensated GPE ($\pm 23.28 \times 10^9$ N/m respectively) using a Laplacian density distribution function, sum these with our GPE estimates and recalculate vertically averaged deviatoric stress. The variations in magnitude are ~2.79 MPa on average, and we find the style of tensors have a misfit of ~0.13 when compared to the vertically averaged deviatoric stress field derived from compensated GPE using equation (6) described below.

3.3. Comparisons With Surface Deformation Indicators

We score our dynamic models by comparing the style of the total vertically averaged deviatoric stress tensors to the style of surface deformation indicators using the following misfit function (Table 1) [*Flesch et al.*, 2007]:

$$M = \frac{1}{2}\left(1 - \frac{\dot{\varepsilon} \cdot \overline{\tau}}{\dot{E}T}\right) \tag{6}$$

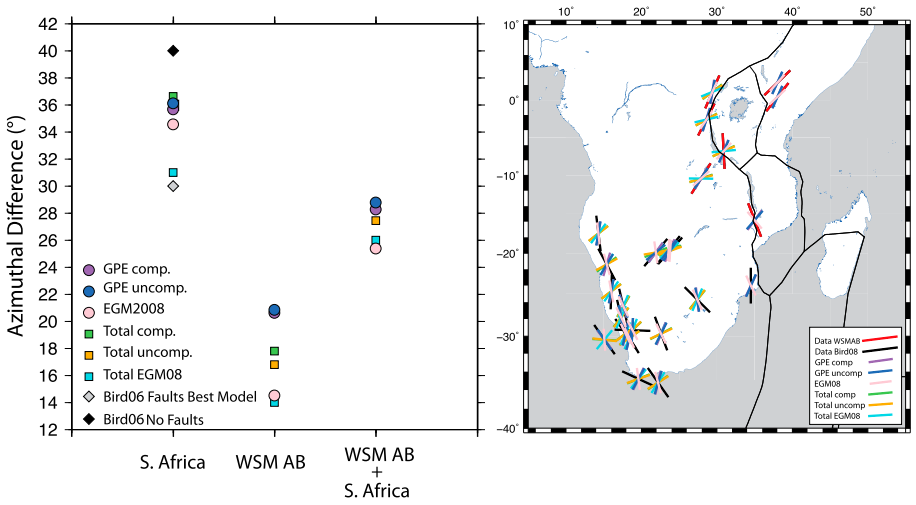

Figure 6. Total vertically averaged deviatoric stress models are represented by squares, circles indicate vertically averaged deviatoric stress from GPE gradients, and diamonds are the 2 models from *Bird et al.* [2006] shown in comparison with the South Africa data. (right) Red lines represent AB quality World Stress Map SH_{max} directions, and blue lines show SH_{max} data from *Bird et al.* [2006] in South Africa. Black lines represent approximate locations of known active faults. (left) Comparison of SH_{max} directions our six models with three data sets: South Africa, WSM AB, and WSM AB + S. Africa.

where $\dot{\varepsilon}$ is strain rate, $\overline{\tau}$ vertically averaged deviatoric stress, $\dot{E}$ the second invariant of strain rate, and T the second invariant of vertically averaged deviatoric stress. A value of 0 indicates tensor alignment and matching styles, while 1 indicates that the model predicts tension where we observe compression (and vice versa) and tensors misalign by 90°.

Near zero strain rate magnitudes result in tensor styles that are unidentifiable. We therefore limit misfit calculations to regions where strain rate magnitudes are above a threshold of 1×10^{-9} yr^{-1}. We derive this threshold from the current level of certainty in GPS velocities (~1 mm/yr) and our model grid size (~100 km).

The misfit plots in Figure 5 show that vertically averaged deviatoric stress fields generated from the CRUST2.0 models provide a better fit overall to the strain rate field ($M = 0.34$) than the model derived from EGM2008 geoid undulations ($M = 0.44$), however, this difference is within the model uncertainty (Table 1). The style of vertically averaged deviatoric stress from both CRUST2.0 models fit surface deformation tensors with a 0.01 difference in misfit. For all three total vertically averaged deviatoric stress models, the lowest misfits occur at oceanic ridges, on the Ethiopian plateau, the Western and Eastern branches of the EARS, and the Rukwa Rift, coincident with zones of extension. The largest misfits occur where plate boundary geometries are poorly understood, i.e., around the Lwandle plate, the triple junction of Rovuma-Nubia-Lwandle, and the Victoria-Nubia-Somalia triple junction. The fit between the stress field indicators and the total vertically averaged deviatoric stress fields improves slightly over the models derived from GPE gradients alone with a decrease in misfit of 0.04–0.05, which is within model error.

3.4. Comparisons With the World Stress Map

We also compare 24 maximum horizontal compressive stress directions (SH_{max}) in eastern and southern Africa from the World Stress Map (WSM) [*Heidbach et al.*, 2008] plus 17 additional SH_{max} stress indicators from the *Bird et al.* [2006] study of South Africa with the vertically averaged deviatoric stress fields calculated in this study (Figure 6). We only use A and B quality stress indicators because the maximum uncertainties are ~15°–20° [*Zoback*, 1992] with one exception from the *Bird et al.* [2006] data set. We separate the data sets into two categories as shown in Figure 6: South Africa (stress data from *Bird et al.* [2006]) and WSM AB (stress data in the EARS).

The differences in azimuths between SH_{max} from the South Africa data set and our models ranges from 31°–37° with the best fit from the total vertically averaged deviatoric stress field derived from EGM2008 geoid undulations. This result compares well with the azimuthal difference of 30° for the best fit *Bird et al.* [2006] model that includes realistic rheologies, faulting, and a force contribution from mantle tractions. A model presented by *Bird et al.* [2006] that does not include faults, which would be the closest comparison

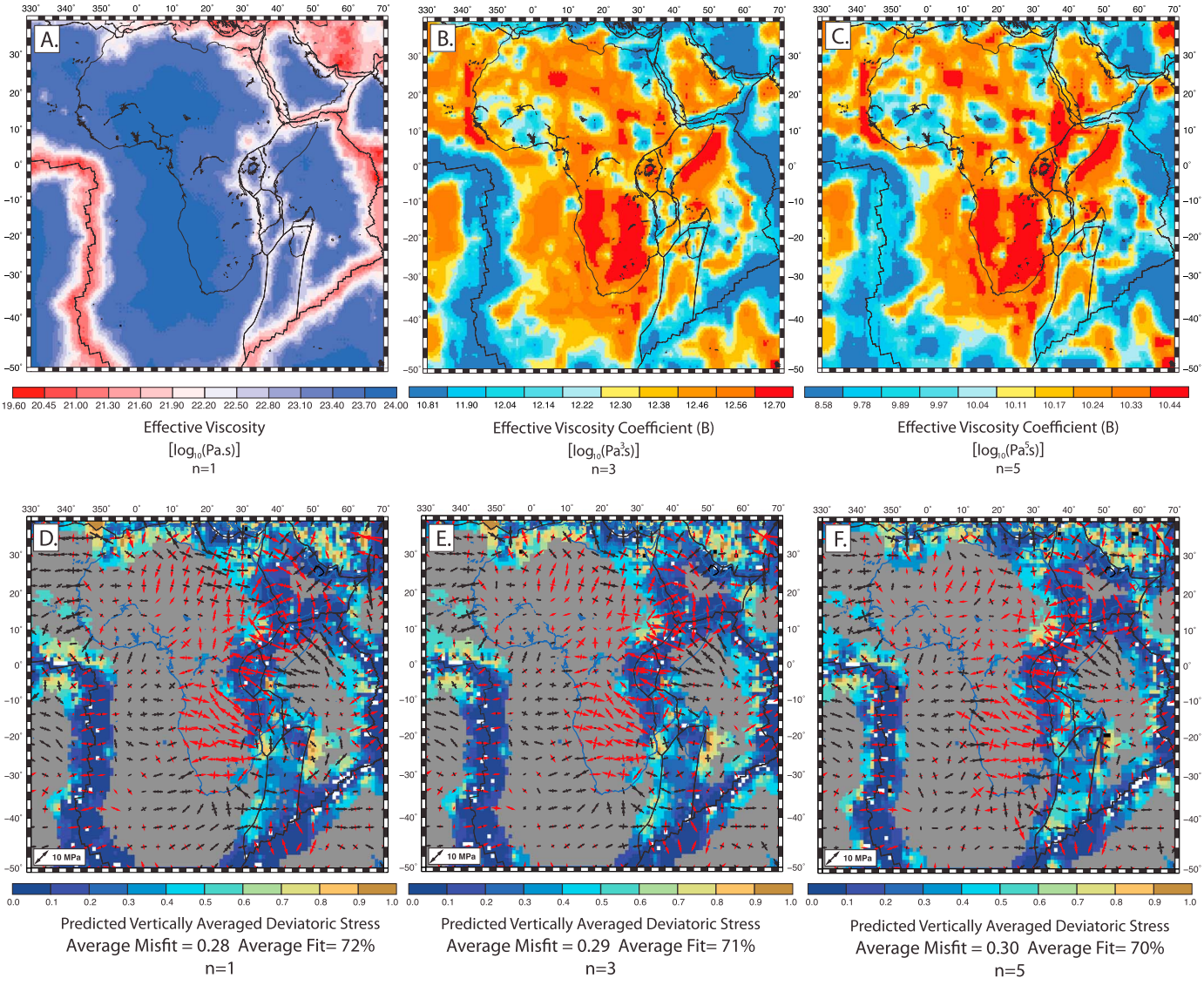

Figure 7. (a) Vertically averaged effective viscosity calculated from the total vertically averaged deviatoric stress for the compensated lithosphere case. This also corresponds to an effective viscosity coefficient with $n = 1$. (b) Effective viscosity coefficient with $n = 3$. (c) Effective viscosity coefficient with $n = 5$. (d–f) The corresponding predicted vertically averaged deviatoric stress fields. The backgrounds are misfit comparisons with stress field indicators from the strain rate field. Gray are regions where strain rates are lower than observational error.

to our work, has a poor fit of 40° and is worse than all of our models. Within the EARS we compare seven available WSM AB indicators with our six models of the total vertically averaged deviatoric stress. SH_{max} azimuthal comparisons are within the uncertainty of WSM SH_{max} ranging from 14° to 18° for all models.

3.5. Vertically Averaged Effective Viscosity

Our vertically averaged minimum total deviatoric stress and strain rate fields provide input for estimates for the lateral variations in vertically averaged effective viscosity. We assume a simple isotropic relationship between total vertically averaged deviatoric stress and strain rates and employ a non-Newtonian constitutive law for viscous flow to calculate vertically averaged effective viscosity and vertically averaged effective viscosity coefficients for Africa and surroundings (Figure 7) using

$$\bar{\eta} = B\dot{E}^{\frac{1}{n}-1} = \frac{T}{\dot{E}} \tag{7}$$

$$B = \frac{\bar{\eta}}{\dot{E}^{\frac{1}{n}-1}}$$

[*England and McKenzie*, 1982] where $\overline{\eta}$ is vertically averaged effective viscosity, B is a viscosity coefficient sensitive to temperature [i.e., *England and McKenzie*, 1982], $\dot{E}$ is the second invariant of strain rate, T is the second invariant of total deviatoric stress for the compensated, uncompensated, or EGM2008-derived GPE models, and n is the power law exponent. Since regions of low strain rate can result in unphysically high effective viscosity magnitudes, we set a maximum effective viscosity estimate of 10^{23} Pa s. As expected, vertically averaged effective viscosity estimates are lower ($10^{19.6}$–$10^{22.5}$ Pa s) at plate boundaries and higher in the interior of tectonic plates ($\geq 10^{23}$ Pa s).

Since effective viscosity is a measure of integrated lithospheric strength, we compare our results with the *Pérez-Gussinyé et al.* [2009] estimates of lithospheric elastic thickness (T_e), an independent measure of strength. Within the Main Ethiopian Rift, in the Eastern branch, most of the Western branch, the Rukwa rift zone, the Victoria-Nubia-Somalia triple junction, and along the Lwandle-Nubia plate boundary low T_e correlates with low $\overline{\eta}$ and active rifting. The broader Ethiopian plateau is evident in both models as a region of low T_e and $\overline{\eta}$. *Pérez-Gussinyé et al.* also find large T_e in the central Victoria, Rovuma, and Lwandle microplates and several regions in Nubia that correlate with cratons and estimates of rigid lithosphere (high $\overline{\eta}$). The uncertainty in the effective viscosity estimates are high, 40% [*Flesch et al.*, 2001]; however, regions of low T_e and low $\overline{\eta}$ that correlate highlight zones of active deformation in the EARS with thinned, weakened lithosphere.

We also calculate an effectivity viscosity ($\overline{\eta}'$) that incorporates a stress field boundary condition contribution amplified by a factor of 10. This effective viscosity model allows us to (1) test a more viscous, stiffer lithosphere and (2) include a stress field boundary condition that is similar in magnitude to the predictions from mantle convection models [i.e., *Ghosh et al.*, 2013].

3.6. Comparison With Deviatoric Stress From Horizontal Mantle Tractions

Because Africa is mostly surrounded by spreading ridges the stress field boundary condition that we determine should represent tractions applied at the base of the thin sheet. Therefore, we interpret that the stress field boundary condition is associated with divergent large-scale mantle flow. Several convection models [e.g., *Conrad and Gurnis*, 2003; *Forte et al.*, 2010; *Steinberger et al.*, 2001] produce a divergent mantle flow pattern beneath the EARS. These models predict tensional deviatoric stresses in the same direction as those produced by GPE since Africa is underlain by the buoyant African Superplume. Our stress field boundary condition may only reflect the minimum magnitude of these deviatoric stresses. This is different from previous estimates of a stress field boundary condition in regions like the India-Eurasian collision, for example, where the stress field boundary condition is the opposite sense of style as deviatoric stresses associated with GPE. In this example the observed deformation represented the trade-off between deviatoric tension and compression and a force balance was able to be uniquely determined. Therefore, we perform two experiments to explore the implications of our stress field boundary condition being a minimum. First, we increase the magnitude of our stress field boundary conditions by a factor of 10 and 100, sum the scaled stress field boundary conditions with the vertically averaged deviatoric stress associated with GPE gradients, compute the misfit to surface observations, and compare the new stress fields with known tectonic regimes in Africa as a proxy for the determining the upper limit of the stress field boundary condition. Increasing the magnitude of the stress field boundary condition by a factor of 10 improves the fit to surface deformation by 5%, and there is no improvement in fit to the strain rate field for the stress field boundary condition amplified by a factor of 100 (Table 1). The improvement in the misfit is within our uncertainty, but the resulting stress fields do not predict compressional stress within the Congo Basin or oceanic basins. Even a small increase in the stress field boundary condition by a factor of two changes compressional stress in the Congo Basin to a strike-slip regime, which suggests the contribution from mantle tractions is small in Africa.

We also qualitatively compare our stress field boundary condition with deviatoric stress output from the *Ghosh et al.* [2013] mantle convection model at 100 km depth (see Appendix, Figure A1e) using the misfit function equation (6) to investigate differences between the two fields. The magnitude of deviatoric stress output from the mantle convection model is on average ~10 times greater than our estimate, but the overall style is tensional across Africa and thus similar to our stress field boundary condition. When we sum the stress field boundary condition associated with the *Ghosh et al.* [2013] mantle convection model with our vertically averaged deviatoric stress from GPE gradients, the fit to surface deformation indicators improves by 7%, but the compressional stress region within the Congo Basin is again not predicted.

These results indicate deviatoric stress associated with GPE gradients fit the patterns of surface deformation in Africa and surroundings in areas where we can resolve strain rates. However, if the pattern of mantle

tractions is in the same direction as that associated with GPE then we are unable to resolve the true magnitude of deviatoric stress associated with basal tractions. Comparing the compressive tectonic regime in the Congo Basin with vertically averaged deviatoric stress suggests basal shear stress must be small or compressive in this region but does not help to constrain the possible magnitudes of basal stress beneath the EARS. It is therefore necessary to perform further dynamic modeling calculations that include a component of rate, and not style alone, in order to estimate the role of horizontal mantle tractions in driving present-day kinematics of Africa and the East African Rift System.

4. Dynamic Velocity, Deviatoric Stress, and Strain Rate Models

4.1. Methodology

To determine the contribution of basal shear tractions in driving surface motions in Africa, we calculate dynamic velocity, deviatoric stress, and strain rate fields that now include a rate component. This dynamic velocity is driven by our vertically averaged effective viscosity distribution, vertically averaged gravitational potential energy or basal shear tractions from large-scale mantle convection, and velocity boundary conditions around the boundary of our grid. We solve the depth averaged 3-D force balance equations now using an estimate of lateral variations in both GPE and effective viscosity by optimizing [*Flesch et al.*, 2001]:

$$\Theta = \int\int_S \left[D + \dot{\varepsilon}_{\gamma\gamma}\overline{\sigma}_{zz}\right] \mathrm{d}x\mathrm{d}y - \int_{\partial S} v_\alpha \overline{\sigma}_{zz} n_\alpha \mathrm{d}l \tag{8}$$

$$D = \frac{n}{n+1} B \left(\dot{\varepsilon}_{\alpha\beta}\dot{\varepsilon}_{\alpha\beta} + \dot{\varepsilon}_{\gamma\gamma}^2\right)^{\frac{n+1}{2n}}$$

where D is the dissipation potential, v_α is the velocity boundary condition from our continuous velocity field solution, and n_α is a unit vector that is perpendicular to the surface around the boundary of ∂S ($\mathrm{d}x\mathrm{d}y$) along $\mathrm{d}l$, and n is the power law exponent. Therefore, with a known distribution of variation in GPE (Figure 3a) and effective viscosity (Figure 7a), we can apply velocity boundary conditions from the kinematic study around the boundary of the grid and calculate the resulting dynamic deviatoric stress, strain rate, and velocity within the interior of our grid for an assumed power law.

We compare the deviatoric stress fields using the compensated CRUST2.0 model to define GPE estimates and assumed power law exponents of 1, 3, and 5 (Figures 7d–7f) with surface deformation indicators from the kinematic strain rate field. We find misfits of 0.3 ± 0.01 for the $n = 1, 3, 5$ cases. On average the maximum difference in magnitude between each predicted deviatoric stress field is ~2 MPa. Additionally, as was shown in *Flesch et al.* [2001], because the B value distributions are updated for each assumed power law this method is unable to determine the power law for the lithosphere but instead shows that the dynamic fields are not dependent on the chosen power law.

We then calculate a dynamic solution resulting from the effect of horizontal mantle tractions output from the *Ghosh and Holt* [2012] convection model using equation (8). This dynamic velocity field includes (1) a velocity boundary condition around the edges of our grid from velocities calculated by *Ghosh and Holt* [2012] that are the result of horizontal mantle tractions on the base of the lithosphere (v_α), (2) vertically averaged effective viscosity with distribution determined by a $B = 1$ (Figure 7a), and (3) the stress response of horizontal tractions acting on the lithosphere from the *Ghosh and Holt* [2012] convection model, which is the negative of tractions and in the mathematical form of GPE [*Ghosh et al.*, 2013] written in spherical coordinates:

$$-r_L^3\sigma_{\Phi r}(r_L) \text{ and } -r_L^3\sigma_{\Theta r}(r_L) \tag{9}$$

The velocity boundary condition is scaled as discussed in *Ghosh and Holt* [2012] supplementary section so that velocities are in units of mm/yr. The resulting dynamic velocity field due to the effect of tractions acting on the lithosphere is larger than calculations of *Ghosh and Holt* [2012] because we have a different effective viscosity distribution and include the Victoria, Rovuma, and Lwandle microplates. Our effective viscosity is based on our more spatially variable strain rate field, which is possible due to the increased availability of GPS observations and inclusion of known microplates. The methods of *Ghosh and Holt* [2012] and this work also differ. We solve the force balance equations regionally with fixed velocity boundary conditions and

Table 2. WRMS Statistics for Dynamic Velocities in NNR Reference Frame at GPS Velocities Along the EAR and on the Somalian Plate [*Saria et al.*, 2013] That Meet the Criteria for Inclusion in Our Kinematic Model[a]

GPE	n	Mantle	Effective Viscosity	WRMS
Compensated	1	n/a	$\bar{\eta}$	2.7
Compensated	3	n/a	$\bar{\eta}$	2.6
Compensated	5	n/a	$\bar{\eta}$	2.7
Compensated	1	yes	$\bar{\eta}$	14.4
Compensated	3	yes	$\bar{\eta}$	13.3
Compensated	5	yes	$\bar{\eta}$	13.3
Compensated	1	n/a	$\bar{\eta}'$	4.0
Compensated	1	yes	$\bar{\eta}'$	5.8
Compensated	1	n/a	$\bar{\eta}_{\text{ridge}} = e^{19}$	3.0
Compensated	1	n/a	$\bar{\eta}_{\text{ridge}} = e^{20}$	3.0
Compensated	1	n/a	$\bar{\eta}_{\text{ridge}} = e^{20.5}$	2.9
Compensated	1	n/a	$\bar{\eta}_{\text{ridge}} = e^{21}$	2.7
Compensated	1	yes	$\bar{\eta}_{\text{ridge}} = e^{19}$	13.2
Compensated	1	yes	$\bar{\eta}_{\text{ridge}} = e^{20}$	13.1
Compensated	1	yes	$\bar{\eta}_{\text{ridge}} = e^{20.5}$	13.1
Compensated	1	yes	$\bar{\eta}_{\text{ridge}} = e^{21}$	13.1
Zero	1	n/a	$\bar{\eta}$	3.7
Zero	1	yes	$\bar{\eta}$	12.4

[a]All models have a velocity boundary condition imposed as described in the text. GPE is the model of gravitational potential energy, n is the power law exponent for the lithosphere, mantle refers to the calculated dynamic velocities from horizontal mantle tractions, ridge refers to the effective viscosity assigned to mid-oceanic ridge where $\bar{\eta}$ is defined in equation (7), $\bar{\eta}'$ is an effectivity viscosity with an amplified contribution of the stress field boundary condition, and WRMS is the fit to GPS velocities in mm/yr.

an absolute effective viscosity distribution, rather than a relative effective viscosity that they use to best fit surface kinematics globally.

In the final step we compute a combined dynamic velocity field. We rotate the dynamic velocity field due to lithospheric buoyancy with $B = 1$ into a no-net-rotation (NNR) reference frame (7.68, −68.44, −0.292°/My) [*DeMets et al.*, 2010] and sum it with that derived from horizontal mantle tractions acting on the lithosphere.

4.2. Results

We quantitatively compare the dynamic velocity fields in an NNR frame with GPS data in the International Reference Frame (ITRF) used in our kinematic model within the EARS and on the Somalian plate [*Saria et al.*, 2013]. We use the WRMS statistic

$$\text{WRMS} = \sqrt{\frac{N}{N-1}\frac{\sum \frac{(V_o - V_m)^2}{\sigma^2}}{\sum \frac{1}{\sigma^2}}} \qquad (10)$$

where V_o is the observed velocity, V_m is dynamic velocity, σ is the uncertainty on the observed data, and N is the number of data used to calculate the WRMS.

Dynamic velocity fields that we calculate from GPE gradients, a velocity boundary condition from our kinematic model, and effective viscosity distributions ($\bar{\eta}$ for $n = 1, 3, 5$) predict plate motions across the EARS with WRMS values of 2.6–2.8 mm/yr (Table 2 and Figure 8a). A solution derived from tractions alone without a contribution from GPE results in velocities that reflect Nubia-Somalia divergence, but the rate is larger by a factor of ∼10 than the observed GPS data (Figure 8b) and resulting WRMS value is 12.4 mm/yr. The combined solution predicts plate motions in the correct direction; however, the magnitudes are again larger than GPS observations of surface motions (Figure 8c). WRMS values are 13.3–14.4 mm/yr and are thus inconsistent with surface kinematics (Table 2). We also repeat this experiment using an effective viscosity model ($\bar{\eta}'$) that is stiffer than $\bar{\eta}$ because we incorporate stress field boundary conditions amplified by a factor of 10. Doing so allows us to test a lithospheric stiffness that may occur if basal shear stress is 10X larger than our estimates as predicted by *Ghosh and Holt* [2012]. For a model without a mantle component the fit to surface observations degrades with an WRMS value of 4.0 mm/yr. A combined solution still over predicts surface observations with an improved WRMS of 5.8 mm/yr (Figures 8d–8f).

To assess the contribution of the imposed velocity boundary condition along the EARS and the Somalian plate, we calculate solutions for (1) a model with zero GPE so that only velocity boundary conditions and lateral variations in effective viscosity drive motions and (2) models with lowered effective viscosity (10^{19}, 10^{20}, $10^{20.5}$, and 10^{21} Pa s) along the Southwest and Central Indian ridges such that the Somalian plate is essentially decoupled from the velocity boundary conditions. In each case we use velocity boundary conditions from the kinematic model presented and rotate the solution into an NNR frame for statistical analysis with GPS velocities in ITRF. When GPE is set to zero we find a WRMS of 3.7 mm/yr (Table 2 and Figure 9h). The low WRMS value for this model does not imply correct velocities across the EARS. Velocities in the Western branch and across the Main Ethiopian Rift are oriented approximately 90° clockwise from present-day E-W extension. This model is only physically meaningful if the Argand number of the lithosphere is large; thus, internal lithospheric buoyancy forces are very small compared to boundary forces. This result illustrates the importance of GPE variations in driving the observed surface deformation field and shows that simple relative movements of plates in our region cannot generate the observed motions. When we lower effective

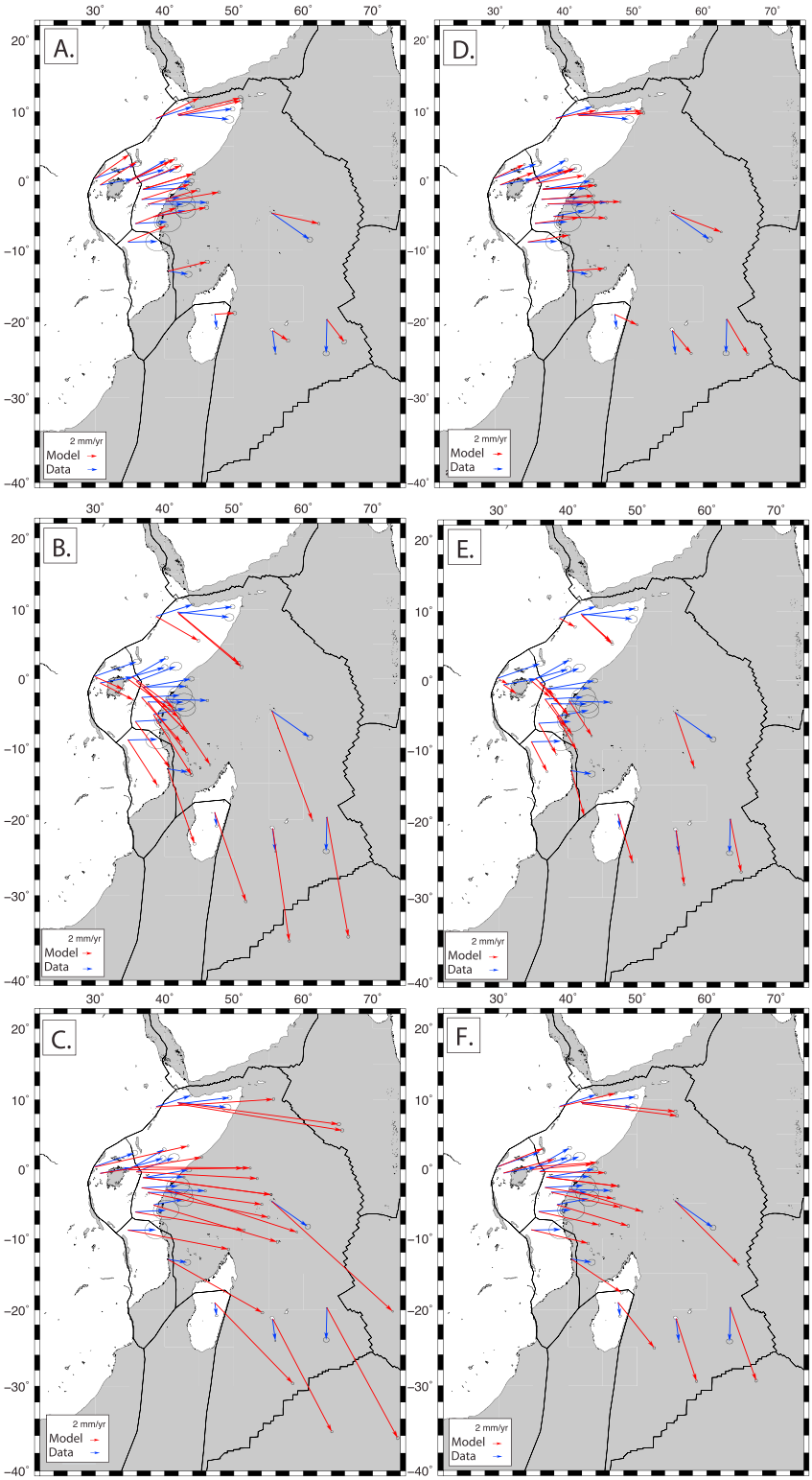

Figure 8. Dynamic velocities for $n = 1$ at GPS site locations rotated into the frame of longitude −20, latitude 20 to highlight plate motions with respect to Nubia in a consistent reference frame. Model velocities are red vectors, and GPS data are blue vectors. (a) Dynamic velocities based on GPE variations, a velocity boundary condition from our surface kinematics model and effective viscosity variations ($\overline{\eta}$). (b) Dynamic velocities based on a velocity boundary condition from *Ghosh and Holt* [2012], effective viscosity variations from this work, and a force contribution from horizontal mantle tractions acting on the lithosphere from *Ghosh and Holt* [2012]. (c) The combined solution. (d–f) Same as Figures 8a–8c but with an effective viscosity model ($\overline{\eta}'$) that includes an amplified stress field boundary condition. See text for details.

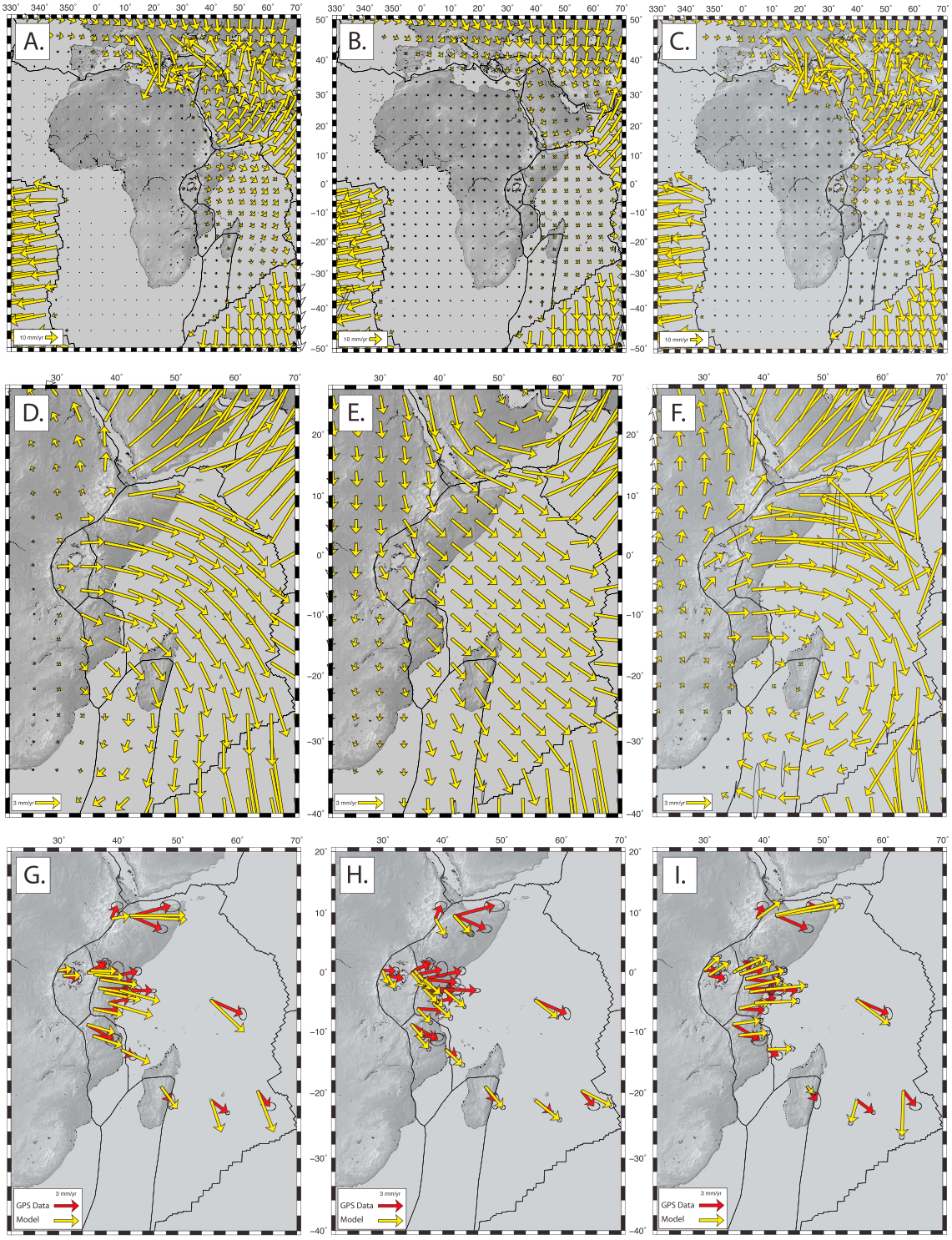

Figure 9. Dynamic velocities ($n = 1$) are yellow vectors and GPS velocities are red. (a) Predicted velocities with input from velocity boundary conditions, effective viscosity, and GPE. (b) Predicted velocities with input from velocity boundary conditions, effective viscosity, and zero GPE. (c) Predicted velocities with input from velocity boundary conditions, effective viscosity lowered to 10^{21} Pa s along the mid-oceanic ridges bounding the Somalian plate, and GPE. (d–f) Same as Figures 9a–9c but focused on the Somalian plate and the EAR. (g–i) Same as above plotted with GPS observations.

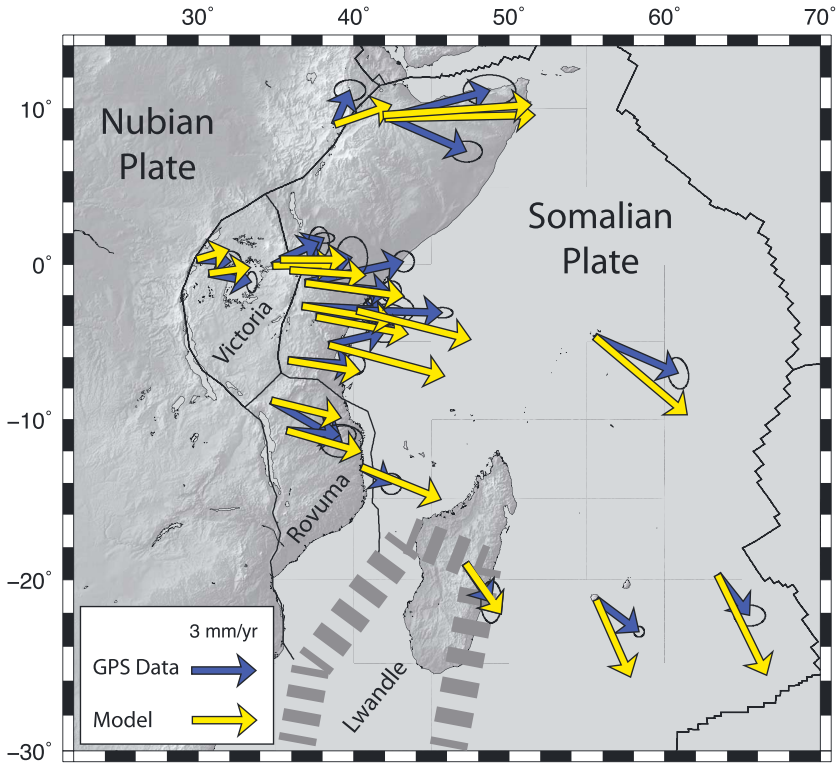

Figure 10. Preferred dynamic velocity model for the East African Rift and the Somalian plate with $n = 3$ and no contribution from horizontal mantle tractions. Predicted velocities are yellow vectors, and GPS data are blue vectors. Uncertainty ellipses are 95% confidence. Both model and velocities are in a Nubia-fixed reference frame.

viscosity along the mid-oceanic ridges, essentially decoupling the motions along the ridges, we find that GPE gradients dominate the rotation of the Somalian plate eastward and torque the Somalian plate clockwise (Figure 9h). Of the four effective viscosities that we test, the lowest WRMS = 2.7 mm/yr occur when the effective viscosity is 10^{21} Pa s along the Southwest and Central Indian ridges. We also add the dynamic velocity field based on horizontal mantle tractions to the decoupled models that we rotate into an NNR frame. This test shows the contribution from horizontal mantle tractions is again too large to explain GPS observations with WRMS values ranging from 13.1 to 13.2 mm/yr.

Our preferred model is driven by our vertically averaged effective viscosity distribution, vertically averaged gravitational potential energy, and velocity boundary conditions from our kinematic model. In Figure 10 we show the preferred model with GPS velocities across the EARS and on the Somalian plate in a Nubia-fixed reference frame. Given our model assumptions, it appears velocities derived from GPE gradients, a velocity boundary condition based on surface kinematics, and an effective viscosity distribution explains the orientation and rate of surface velocities without the need for tractions from viscous coupling to an active mantle dominating the force balance. However, it is important to note that while dynamic velocities driven by the effects of tractions acting at the base of the lithosphere over predict observed surface motions, our results suggest some component of basal tractions contribute to the force balance at a reduced level. For example, the applied velocity boundary condition contains the integrated effects of global tractions to the boundary of our grid and does play an important role in the movement of plates surrounding the EARS [i.e., *Ghosh and Holt*, 2012] and could help drive a possible component of ridge-coupling needed to control the rotation of the Somalian plate. Additionally, dynamic velocities resulting from the input of the traction potential in the EARS produce an overestimate of dynamic velocity directed more southward than observed Figure 8b, while the solution driven by GPE alone produces dynamic velocities rotated more northward than observed Figure 8a. A combination of reduced contribution of dynamic velocities associated with basal tractions on the order of 2 mm/yr could slightly reorient the dynamic velocities in the EARS driven by GPE variation alone to improve the fit to GPS observations. However, because the traction field used here comes from a best fit global model, we are unable to estimate a reduced traction response because decreasing asthenospheric

viscosity beneath the EARS will have implications globally that may or may not be physically realistic [*Ghosh and Holt*, 2012]; thus, we can only say qualitatively that a contribution on the order of a magnitude lower than produced here could add to the force balance in the EARS. We have quantitatively shown that (1) tractions over predict surface motions and (2) a model that is decoupled from the surrounding plates and with no contribution from mantle tractions results in the correct magnitude but a small northward component that is not evident in the GPS observations and a spinning of the Somalian plate. In our preferred model this northward component rotates in the correct SE orientation, which we attribute to a small addition of basal tractions that we model here or more coupling and pull from the Southwest Indian Ridge. We incorporate ridge coupling into the velocity boundary condition that can mimic the needed traction; however, in the preferred model we do not apply tractions to the base of the lithosphere using the velocity boundary conditions except at the boundary.

5. Discussion

5.1. Role of Large-Scale Mantle Convection

Forte et al. [2010] recently proposed that divergent flow associated with the South and West African Superplumes under Africa efficiently couples with the lithosphere, inducing tensional stresses which, in turn, drive opening of the EARS. This implies that deviatoric stress from GPE gradients within the lithosphere are not currently playing a dominant role in sustaining continental rifting in East Africa. The *Forte et al.* [2010] result is consistent with a recent study by *Ghosh and Holt* [2012] who find mantle tractions alone beneath Africa are insufficient to reproduce surface observations. Both studies suggest lithospheric buoyancy is required to explain present-day plate motions. *Ghosh and Holt* [2012] model fit to observed velocities improves when they incorporate the contribution of lithospheric buoyancy forces. In our model, the stress field boundary condition, which we infer to represent the contribution from divergent large-scale mantle flow, adds only 1–2 MPa of deviatoric tension.

Since tomography studies unanimously detect the African Superplume *Zhao*[2007, and references therein], we expect large-scale mantle flow beneath Africa, with upward and divergent flow under eastern Africa, as modeled for example by *Behn et al.* [2004], *Forte et al.* [2010], *Moucha and Forte* [2011], and *Buiter et al.* [2012]. Since we find that viscous coupling to our modeled active mantle flow over predicts surface velocities, we propose two hypotheses about the mantle-lithosphere coupling beneath Africa. (1) Viscous coupling between mantle flow and the lithosphere is not efficient beneath the EARS, although small-scale convection and localized coupling could play a role. Inefficient coupling, in turn, would require lower than average asthenospheric viscosity under Africa and the EARS in particular that is supported by evidence of higher than average upper mantle temperatures and wet olivine upper mantle rheology. Seismic tomography [*Priestley et al.*, 2008], *P* wave spectral amplitude ratios [*Venkataraman et al.*, 2004], and petrology studies [e.g., *Janney et al.*, 2010; *Rooney et al.*, 2011] suggest the upper mantle has higher than average temperatures beneath East African Rift System branches, oceanic regions surrounding Africa, off-craton regions in South Africa, and possibly all of Africa except for small regions beneath the West African, Congo, Kaapvaal, and Tanzania cratons. Although cratonic roots in some regions may have lower temperatures, *Lee et al.* [2011, and references therein] present geochemical evidence from kimberlite nodules of the Tanzania and Kaapvaal cratons that suggest their roots are hydrated which could promote low-viscosity asthenosphere. (2) An alternative explanation is that mantle flow may not be as vigorous in the upper mantle as expected which would mean kimberlites sample local anomalies in the mantle and do not represent regional-scale upper mantle geochemistry.

5.2. Total Stress Versus Strength of the Lithosphere

A logical next step is to assess whether the total vertically averaged deviatoric stress field described above is capable of initiating the rupture of continental lithosphere in East Africa. *Kusznir and Park* [1984] and *Hopper and Buck* [1993] pointed out that the tectonic force required to initiate and maintain breakup of thick continental lithosphere are up to an order of magnitude larger than available. *Buck* [2004] proposes that magma intrusion is needed to weaken the lithosphere and provide the additional buoyancy force required to reach rupture. Dike intrusions in the early evolution of cratonic rifts support that hypothesis [e.g., *Calais et al.*, 2008].

To address the issue of forces available versus strength of the lithosphere, we compute vertically averaged lithospheric strength in two ways, first at the large scale and second at the local scale. In both cases we

Table 3. Input Parameters for Lithospheric Strength Calculations. GHFD = Global Heat Flow Database (See Text for Reference)[a]

Parameter	Crust		Mantle
Density (kg/m^3)	CRUST2.0		variable
Stress exponent (n)		3	
Friction coefficient (f)		0.1	
Biot coefficient		1	
Moho depth (m)	CRUST2.0		n/a
Thermal conductivity (W/m K)	2.7		3.2
Radioactive heat production (W/m^3)	3.5×10^{-7}		3.2×10^{-8}
Volumetric thermal expansion (K^{-1})	2.4×10^{-5}		3.9×10^{-5}
Surface heat flow (W/m^2)		interpolated GHFD	
Strain rate (s^{-1})		spatially varying—this work	
1/A (Pa $s^{-1/n}$)	2.3×10^{8}		9.5×10^{4}
E^*/nR (K)	1.1×10^{4}		18314
Va/nR (K/m)	0		0.0171

[a]A = preexponential factor, R = universal gas constant, E^* = activation energy, Va = activation volume. In *Bird et al.* [2008], $1/A$ = ACREEP, E^*/nR = BCREEP, Va/nR = CCREEP.

assume a Coulomb friction law for the brittle crust [i.e., *Bird*, 1998]:

$$\tau^{\text{friction}} = f\left[gz(\rho_{c/m} - B\rho_{\text{water}}) + \sigma_{zz}\right] \tag{11}$$

and a flow law (dislocation creep) for the lower crust and for viscous rheology in the mantle-lithosphere [i.e., *Bird*, 1998]:

$$\tau^{\text{creep}} = A\dot{\epsilon}^{\frac{1-n}{n}} \exp\left[\frac{E + V_a z}{nRT(z)}\right] \tag{12}$$

$$= (\text{ACREEP})\dot{\epsilon}^{(\text{ECREEP}-1)} e^{[(\text{BCREEP}+\text{CCREEP}\times z)/T(z)]} \tag{13}$$

(see Table 3 for input values and definitions).

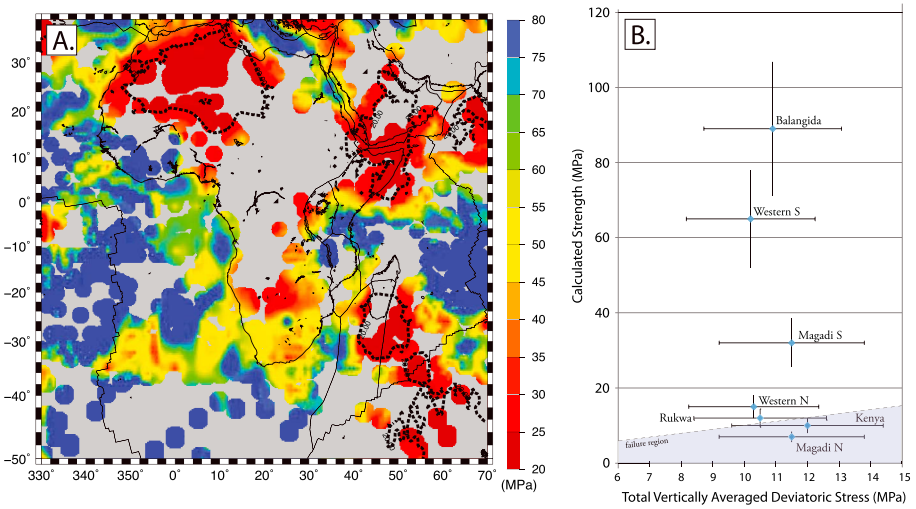

Figure 11. (a) Vertically averaged lithospheric strength derived from an explicit calculation assuming a Coulomb friction law for the brittle crust and a flow law (dislocation creep) for the lower crust and mantle-lithosphere. Parameters are provided in Table 2. Regions with no heat flow data are masked. For comparison with tectonic stress estimated in this work, we show 20 MPa contour intervals with dashed lines. (b) Calculated vertically integrated strength of the lithosphere at specific regions within the EARS as a function of the total vertically integrated stress (or total stress) at the same locations. A 20% average standard deviation is assigned to each estimate to account for uncertainties in rheological parameters used to calculate lithospheric strength. The dashed line corresponds to calculated strength = total vertically averaged deviatoric stress. Grey area below this line show area where total vertically averaged deviatoric stress is sufficient to cause lithospheric failure.

Table 4. Rheological Parameters (Crust Only) and Results for Lithospheric Strength Calculations in Specific Regions of the EARS[a]

Location	Heat Flow (mW/m^2)	Moho (km)	$1/A$ ($Pa\ s^{-1/n}$)	E^*/nR (K)	Yield Stress (MPa)	Tectonic Stress (MPa)
Magadi N.	103.4	20	5.78×10^5	3,841.29	7	11.5
Bogoria	103.4	30	2.97×10^7	8,779.90	10	12
Rukwa	71.3	40	1.5×10^7	9,822.00	12	10.5
Western N.	73.1	33	4.8×10^7	9,621.80	15	10.3
Magadi S.	103.4	26	2.28×10^{32}	160.40	32	11.5
Western S.	67.4	43	2.78×10^{32}	160.40	65	10.2
Balangida	46.0	37	6.66×10^7	10,423.60	89	10.9

[a]Mantle-lithosphere parameters and Va/nR are listed in Table 3. Locations are defined in Figure 1d.

At the large scale we use friction coefficient and flow parameter values derived from rock mechanics experiments (Table 3) [*e.g., Tullis*, 1971; *Weertman and Weertman*, 1975; *Kirby*, 1983]. These strength calculations also incorporate interpolated heat flow derived from the Global Heat Flow Database [*Hasterok*, 2010] and *Nyblade et al.* [1990], strain rates from this work, crustal thicknesses and density from CRUST2.0, and mantle-lithosphere density heterogeneities calculated such that the lithosphere is in isostatic balance (Figure 11a). We find an integrated lithospheric strength ranging from ~30 to 80 MPa in the EARS (corresponding to a cumulative force of 3 to 8 TN/m for a 100 km thick lithosphere) with the exception of the Red Sea and Gulf of Aden where integrated strength is ~20 MPa. In most of the EARS, the integrated lithospheric strength is therefore significantly larger than the tectonic stresses estimated in this work (~10–22 MPa per 100 km thick lithosphere or a cumulative force of 1–2.2 TN/m). This calculation shows that the continental lithosphere in most of eastern Africa is too strong to be ruptured by the tectonic stresses estimated in this work. This poses a problem for many traditional models of rifting, where rupture occurs only as a result of tectonic forces in simple shear [e.g., *Wernicke*, 1981; *Lister et al.*, 1986] or pure shear [e.g., *McKenzie*, 1978; *Rowley and Sagahain*, 1986; *Knoll et al.*, 2009].

This result may also mean that the generic parameters used above to calculate vertically integrated lithospheric strength are not adapted to the specific geophysical context of the EARS. Recent seismological studies have indeed shown significant regional variations of the thermomechanical properties of the lithosphere along the EARS, with an increase in lithospheric strength from north to south along the eastern branch [e.g., *Albaric et al.*, 2009; *Yang and Chen*, 2010]. We therefore calculate vertically averaged lithospheric strength in nine regions of the central EARS where *Albaric et al.* [2009] determined local crustal rheology using seismicity depth distribution (Western branch north and south, Rukwa Rift, Balangida Rift, Malawi Rift, Magadi Rift north and south, and Kenya Rift (Bogoria)). In these regions we calculate the integrated strength of a 100 km thick lithosphere using local heat flow data from *Nyblade et al.* [1990], flow law parameters for crustal and mantle material from *Ranalli* [1997], *Turcotte and Schubert* [2002], and *Afonso and Ranalli* [2004], and crustal thicknesses defined by maximum earthquake cutoff [*Albaric et al.*, 2009]. We find that the vertically integrated strength of the lithosphere is lower than available tectonic forces (total vertically averaged deviatoric stress) in relatively limited areas: the Kenya Rift, the northern part of the Magadi Rift, and a segment of the Rukwa Rift (Table 4 and Figure 11b).

Therefore, if the lithosphere has been weakened or thinned, for instance, via heat advection from small-scale convection, as proposed by *Davis and Slack* [2002] under the Kenya dome, then currently available tectonic stresses are sufficient to initiate rifting. In addition, once melt is present, the additional buoyancy force provided through dike intrusions also contributes to reducing the force necessary for extensional yielding [*Buck*, 2004]. The recent evidence for shallow magmatic intrusions and diking at the southern end of the Eastern Branch in the Natron Rift *Calais et al.* [2008] indicate that this process may be contributing to rift propagation into the cold, thick, Tanzanian craton. However, this model does not explain rifting in the Western Branch and the Malawi Rift, where heat flow is close to that of a normal lithosphere. In these locations, and perhaps others, forcing from the flow of plume material beneath individual rifts with variable thickness may also play a role in active rifting, which we do not address with this work given our modeling assumptions.

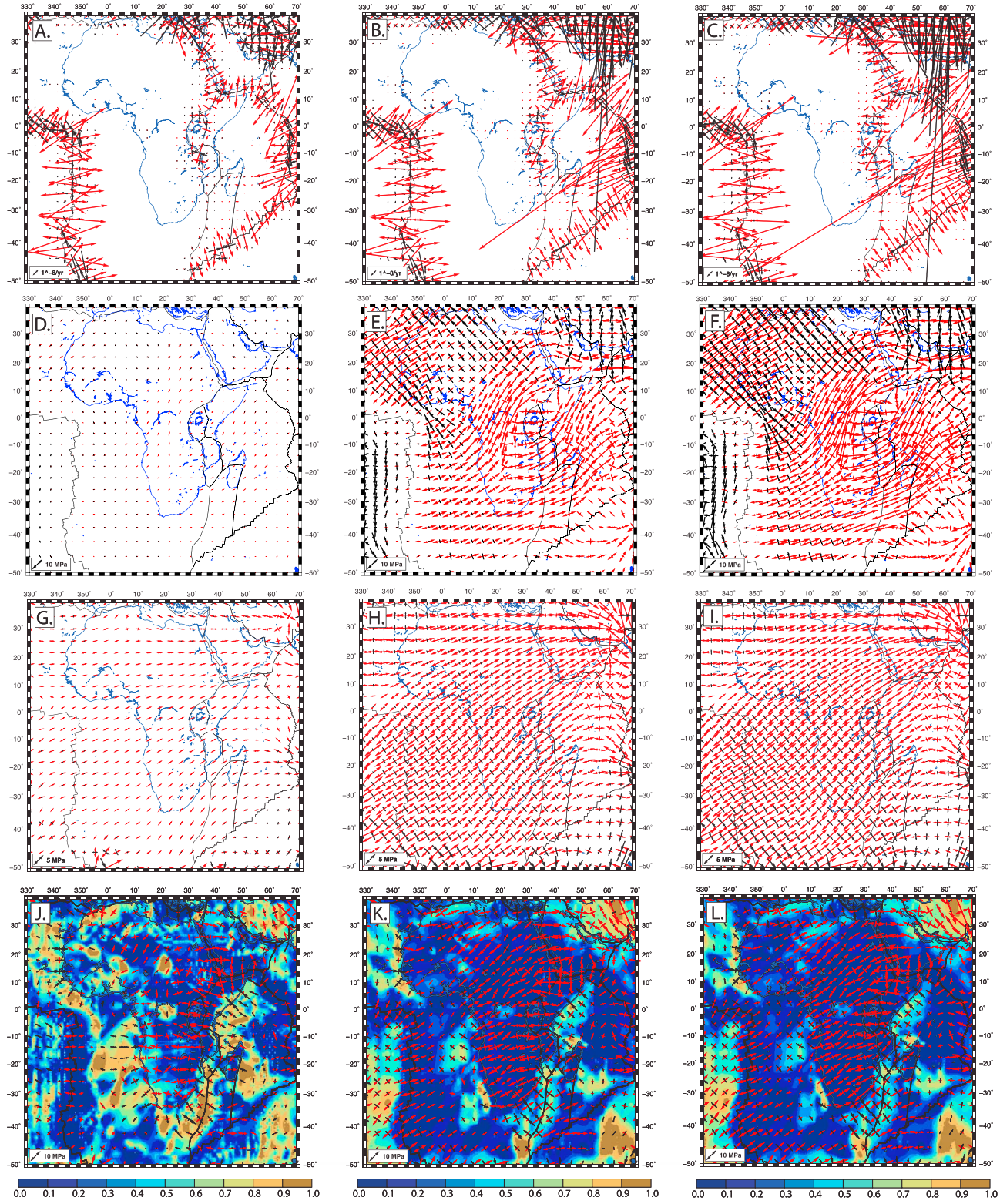

Figure A1. (a) Synthetic strain rate field with $c = 0.1$. (b) Same as Figure A1a for $c = 1.0$. (c) Same as Figures A1a and A1b but for $c = 1.5$. (d) Scaled deviatoric stress from horizontal tractions of *Ghosh et al.* [2013] at 100 km depth for $c = 0.1$. (e) Same as Figure A1d but for $c = 1.0$. (f) Same as Figures A1d and A1e but for $c = 1.5$. (g) Stress field boundary condition that best fits the synthetic strain rate field with $c = 0.1$ using a compensated model of vertically average deviatoric stress from GPE gradients. (h) Same as Figure A1g but for $c = 1.0$. (i) Same as Figures A1h and A1g but for $c = 1.5$. (j) Total vertically averaged deviatoric stress for the based on the best fit stress field boundary condition for the synthetic strain rate deformation tensors with $c = 0.1$. (k) Same as Figure A1g but for $c = 1.0$. (l) Same as Figures A1g and A1h but for $c = 1.5$.

6. Conclusions

At a global scale, *Ghosh et al.* [2008] suggest that basal tractions from large-scale mantle convection contribute on average 50% of the total deviatoric stress field in the lithosphere. Our study indicates that mantle contribution to lithospheric stresses in Africa may be lower than their global estimations and that buoyancy forces likely dominate the lithospheric force budget. Given our modeling assumptions, this work suggests an active role of horizontal mantle tractions is not required to fit observations of plate motions along the EARS and on the Somalian plate. The results we present here indicate lithospheric deformation in Africa is currently driven mostly by horizontal gradients in GPE that include epierogenic effects from the African Superplume. We further argue that total vertically averaged deviatoric stress is insufficient to rupture unaltered continental lithosphere over most of Africa, thus additional processes that reduce the strength of the lithosphere are required to initiate rifting in the EARS. This conclusion quantifies, for the EARS, the "stress paradox," where forces available from tectonic sources are insufficient to break an initially thick, cold lithosphere [*Buck*, 2004]. The intrusion of magmatic dikes, which decrease rupture yield stress, may be required to initiate continental breakup in regions of unaltered lithosphere [*Buck*, 2004]. Alternatively, the lithospheric strength calculated here may be too large in rift areas, where the lithosphere has been weakened by faulting from previous orogenies [i.e., *Wijk*, 2005], magmatic intrusions [*Walker et al.*, 2004; *Gao et al.*, 1997], and/or may have undergone thermal erosion from asthenospheric upwellings [e.g., *Green et al.*, 1991; *Ritsema et al.*, 1998; *Davis and Slack*, 2002].

Appendix A: Resolving Long-Wavelength Strain Rate Signals in the Stress Field Boundary Condition

In Africa the stresses from GPE and large-scale horizonal mantle tractions may be in the same direction. We investigate the sensitivity of small additions of tractions in the strain rate solution and test the resolution of the basis functions to reproduce stress associated with these basal tractions. We add a series of synthetic long-wavelength strain rate signals derived from basal shear tractions of a mantle convection model [*Ghosh et al.*, 2013] to our kinematic strain rate field and invert for a new stress field boundary condition. We calculate the synthetic long-wavelength strain rate field contribution assuming

$$\dot{\varepsilon}' = \dot{\varepsilon}_o + c\frac{\tau_m}{\overline{\eta}} \tag{A1}$$

where $\dot{\varepsilon}'$ is the new, synthetic strain rate field, $\dot{\varepsilon}_o$ is our observed strain rate field (Figure 2), $\overline{\eta} = T/\dot{E}$, which represents an effective viscosity based on the total deviatoric compensated stress field (Figure 5g), c is a scaling factor, and τ_m is vertically integrated horizontal deviatoric stress at 100 km depth from the mantle convection model calculated by *Ghosh et al.* [2013]. We generated three synthetic strain rate fields scaled by c = 0.1, 1.0, and 1.5 (Figures A1a–A1c) that have an additional long-wavelength signal from the *Ghosh et al.* [2013] horizontal mantle traction field (Figures A1d–A1f prior to division by $\overline{\eta}$). We applied the methods described above to calculate stress field boundary conditions (Figures A1g–A1i), total deviatoric stress fields (Figures A1j–A1l), and the corresponding misfit calculations described in section 3.3 (backgrounds in Figures A1j–A1l) for each synthetic observed deformation field. Indeed, the patterns and magnitudes of the stress field boundary conditions reflect the additional long-wavelength signal in $\dot{\varepsilon}'$. The magnitude of the stress field boundary condition increases as we increase the magnitude of the synthetic strain signal from the mantle. The pattern also changes. For the stress field boundary condition derived from fitting the tensor styles of $\dot{\varepsilon}'$ with $c = 0.1$ shows pure tensional deviatoric stresses across the Nubian plate, whereas a NW-SE oriented compressional component is evident for stress field boundary conditions of $\dot{\varepsilon}'$ with $c = 1.0$ and 1.5. These tests validate the effectiveness of this method to resolve a long-wavelength signal in the strain rate field if it is indeed included.

Acknowledgments
This work was funded by NSF grant EAR-0538119 and the NSF Graduate Research Fellowship program grant 2009052513. We thank reviewers Gene Humphreys and Peter Bird for comments that improved an earlier version of this work, and we thank Norm Sleep and an anonymous reviewer for suggestions that markedly improved this manuscript. We also thank Jay Melosh and Hersh Gilbert for feedback and reviews, Carolina Lithgow-Bertelloni, Bernhard Steinberger, and Alessandro Forte for providing data for model comparisons, and Tiku Ravat for insightful discussion about this work. GPS data used in this work are archived at UNAVCO (www.unavco.org).

References

Adams, A., A. Nyblade, and D. Weerarane (2012), Upper mantle shear wave velocity structure beneath the East African plateau: Evidence for a deep, plateauwide low velocity anomaly, *Geophys. J. Int.*, *189*, 123–142, doi:10.1111/j.1365-246X.2012.05373.x.

Afonso, J. C., and G. Ranalli (2004), Crustal and mantle strengths in continental lithosphere: Is the jelly sandwich obsolete?, *Tectonophysics*, *394*, 221–232, doi:10.1016/j.tecto.2004.08.006.

Albaric, J., J. Déverchére, J. P. C. Petit, and B. L. Gall (2009), Crustal rheology and depth distribution of earthquakes: Insights from the Central and Southern East African Rift system, *Tectonophysics*, *468*(1–4), 28–41, doi:10.1016/j.tecto.2008.05.021.

Amelung, F., and G. King (1997), Large-scale tectonic deformation inferred from small earthquakes, *Nature*, *386*, 702–705.
Artushkov, E. V. (1973), Stresses in the lithosphere caused by crustal thickness inhomogeneities, *J. Geophys. Res.*, *78*(32), 7675–7708.
Bassin, C., G. Laske, and G. Masters (2000), The current limits of resolution for surface wave tomography in North America, *Eos Trans. AGU*, *81*, Fall Meet. Suppl., Abstract F897.
Bastow, I. D., G. W. Stuart, J.-M. Kendall, and C. J. Ebinger (2005), Upper-mantle seismic structure in a region of incipient continental breakup: Northern Ethiopian Rift, *Geophys. J. Int.*, *162*, 479–493, doi:10.1111/j.1365-246X.2005.02666.x.
Behn, M. D., C. P. Conrad, and P. G. Silver (2004), Detection of upper mantle flow associated with the African Superplume, *Earth Planet. Sci. Lett.*, *224*, 259–274.
Bird, P. (1998), Testing hypotheses on plate-driving mechanisms with global lithosphere models including topography, thermal structure, and faults, *J. Geophys. Res.*, *103*(B5), 10,115–10,129.
Bird, P., and K. Piper (1980), Plane-stress finite-element models of tectonic flow in southern California, *Phys. Earth Planet. Inter.*, *21*(2–3), 158–175.
Bird, P., Z. Ben-Avraham, G. Schubert, M. Andreoli, and G. Viola (2006), Patterns of stress and strain rate in Southern Africa, *J. Geophys. Res.*, *111*, B08402, doi:10.1029/2005JB003882.
Bird, P., Z. Liu, and W. K. Rucker (2008), Stresses that drive the plates from below: Definitions, computational path, model optimization, and error analysis, *J. Geophys. Res.*, *113*, B11406, doi:10.1029/2007JB005460.
Buck, R. W. (2004), Consequences of asthenospheric variability on continental rifting, in *Rheology and Deformation of the Lithosphere at Continental Margins*, edited by G. D. Karner et al., pp. 1–30, Columbia Univ. Press, New York.
Buiter, S. J. H., B. Steinberger, S. Medvedev, and J. L. Tetreault (2012), Could the mantle have caused subsidence of the Congo Basin?, *Tectonophysics*, *514*, 62–80.
Calais, E., C. J. Ebinger, C. Hartnady, and J.-M. Nocquet (2006), Kinematics of the East African Rift from GPS and earthquake slip vector data, in *The Afar Volcanic Province Within the East African Rift System*, vol. 259, edited by G. Yirgu, C. J. Ebinger, and P. K. H. Maguire, pp. 9–22, Geol. Soc. Spec. Publ., London.
Calais, E., et al. (2008), Strain accommodation by slow slip and dyking in a youthful continental rift, East Africa, *Nature*, *456*, 783–787, doi:10.1038/nature07478.
Coblentz, D. D., and M. Sandiford (1994), Tectonic stresses in the African plate: Constraints on the ambient lithospheric stress state, *Geology*, *22*, 831–834.
Coblentz, D. D., R. M. Richardson, and M. Sandiford (1994), On the gravitational potential of the Earth's lithosphere, *Tectonics*, *13*, 929–945.
Conrad, C. P., and M. Gurnis (2003), Seismic tomography, surface uplift, and the breakup of Gondwanaland: Integrating mantle convection backwards in time, *Geochem. Geophys. Geosyst.*, *4*(3), 1031, doi:10.1029/2001GC000299.
Craig, T. J., J. A. Jackson, K. Priestley, and D. McKenzie (2011), Earthquake distribution patterns in Africa: Their relationship to variations in lithospheric and geological structure, and their rheological implications, *Geophys. J. Int.*, *185*, 403–434, doi:10.1111/j.1365-246X.2011.04950.x.
Davis, P., and P. D. Slack (2002), The uppermost mantle beneath the Kenya dome and relation to melting, rifting and uplift in East Africa, *Geophys. Res. Lett.*, *29*(7), 1117, doi:10.1029/2001GL013676.
Delvaux, D., and A. Barth (2010), African stress pattern from formal inversion of focal mechanism data, *Tectonophysics*, *482*, 105–128.
DeMets, C., R. G. Gordan, and D. F. Argus (2010), Geologically current plate motions, *Geophys. J. Int.*, *181*, 1–80, doi:10.1111/j.1365-246X.2009.04491.x.
Dziewonski, A. M., T.-A. Chou, and J. H. Woodhouse (1981), Determination of earthquake source parameters from waveform data for studies of global and regional seismicity, *J. Geophys. Res.*, *86*, 2825–2852.
Dziewonski, A. M., G. Ekström, and M. P. Salagnik (1996), Centroid-moment tensor solutions for July–September 1995, *Phys. Earth Planet. Inter.*, *97*, 3–13.
England, P., and D. P. McKenzie (1982), A thin viscous sheet model for continental deformation, *Geophys. J. R. Astron. Soc.*, *70*, 321–395.
Finzel, E., L. M. Flesch, and K. D. Ridgeway (2011), Kinematics of a diffuse North America-Pacific-Bering plate boundary in Alaska and western Canada, *Geology*, *39*(9), 835–838, doi:10.1130/G32271.1.
Flesch, L. M., W. E. Holt, A. J. Haines, and B. Shen-Tu (2000), Dynamics of the Pacific-North American plate boundary in the western United States, *Science*, *834*, 834–836, doi:10.1126/science.287.5454.834.
Flesch, L. M., J. A. Haines, and W. E. Holt (2001), Dynamics of the India-Eurasia collision zone, *J. Geophys. Res.*, *106*, 16,435–16,460.
Flesch, L. M., W. E. Holt, A. J. Haines, L. Wen, and B. Shen-Tu (2007), The dynamics of Western North America: Stress magnitudes and the relative role of gravitational potential energy, plate interaction at the boundary, and basal tractions, *Geophys. J. Int.*, *169*, 866–896, doi:10.1111/j.1365-246X.2007.03274.x.
Forsyth, D., and S. Uyeda (1975), On the relative importance of the driving forces of plate motion, *Geophys. J. R. Astron. Soc.*, *43*, 163–200.
Forte, A. M., M. S. Quéré, R. Moucha, N. A. Simmons, S. P. Grand, J. X. Mitrovica, and D. B. Rowley (2010), Joint seismic-geodynamic-mineral physical modeling of African geodynamics: A reconciliation of deep-mantle convection with surface geophysical constraints, *Earth Planet. Sci. Lett.*, *295*, 329–341, doi:10.1016/j.epsl.2010.03.017.
Gao, S., P. M. Davis, H. Liu, P. D. Slack, A. W. Rigor, Y. A. Zorin, V. V. Mordvinova, V. M. Kozhevnikov, and N. A. Logatchev (1997), SKS splitting beneath continental rift zones, *J. Geophys. Res.*, *102*(B10), 22,781–22,797.
Ghosh, A., and W. Holt (2012), Plate motions and stresses from global dynamic models, *Science*, *335*(838–843), doi:10.1126/science.1214209.
Ghosh, A., W. E. Holt, L. Wen, A. J. Haines, and L. M. Flesch (2008), Joint modeling of lithosphere and mantle dynamics elucidating lithosphere-mantle coupling, *Geophys. Res. Lett.*, *35*, L16309, doi:10.1029/2008GL034365.
Ghosh, A., W. E. Holt, and L. M. Flesch (2009), Contribution of gravitational potential energy differences to the global stress field, *Geophy. J. Int.*, *179*, 787–812, doi:10.1111/j.1365-246X.2009.04326.x.
Ghosh, A., W. E. Holt, and L. M. Wen (2013), Predicting the lithospheric stress field and plate motions by joint modeling of lithosphere and mantle dynamics, *J. Geophy. Res. Solid Earth*, *118*, 346–368, doi:10.1029/2012JB009516.
Green, W. V., U. Achauer, and R. P. Meyer (1991), A three-dimensional seismic image of the crust and upper mantle beneath the Kenya Rift, *Nature*, *354*, 199–203, doi:10.1038/354199a0.
Hager, B. H., and R. J. O'Connell (1981), A simple global model of plate dynamics and mantle convection, *J. Geophys.*, *86*(B6), 4843–4867.
Haines, A. J., and W. E. Holt (1993), A procedure for obtaining the complete horizontal motions within zones of distributed deformation from the inversion of strain rate data, *J. Geophys Res.*, *98*(B7), 12,057–12,082.
Haines, A. J., W. E. Holt, and D. C. Agnew (1998), Representing distributed deformation by continuous velocity fields, *Sci. Rept. 98/5*, Inst. of Geol. and Nucl. Sci., Wellington, N. Z.
Hartnady, C. (2002), Earthquake hazard in Africa: Perspectives on the Nubia-Somalia boundary, *S. Afr. J. Sci.*, *98*, 425–428.

Hasterok, D. (2010), Thermal regime of the continental and the oceanic lithosphere, PhD thesis, Dept. of Geol. and Geophys., Univ. of Utah, Salt Lake City, Utah.
Heidbach, O., M. Tingay, A. Barth, J. Reinecjer, B. D. Kurfeß, and B. Müller (2008), The World Stress Map based on the database release 2008, equatorial scale 1:46,000,000, Commission for the Geological Map of the World, Paris. [Available at http://www.world-stress-map.org.]
Holt, W. E., and A. J. Haines (1995), The kinematics of Northern South Island New Zealand determined from geologic strain rates, *J. Geophys. Res.*, *100*, 17,991–18,010.
Hopper, J. R., and W. R. Buck (1993), The initiation of rifting at constant tectonic force: The role of diffusion creep, *J. Geophys. Res.*, *98*(16), 16,213–16,221.
Horner-Johnson, B. C., R. G. Gordon, and D. F. Argus (2007), Plate kinematic evidence for the existence of a distinct plate between the Nubian and Somalian plates along the Southwest Indian Ridge, *J. Geophys. Res.*, *112*, B05418, doi:10.1029/2006JB004519.
Janney, P. E., S. B. Shirey, R. W. Carlson, D. G. Pearson, D. R. Bell, A. P. L. Roex, A. Ishikawa, P. H. Nixon, and F. R. Boyd (2010), Age, composition and thermal characteristics of South African off-craton mantle lithosphere: Evidence for a multi-stage history, *J. Petro.*, *51*(9), 1849–1890, doi:10.1093/petrology/egq041.
King, S. (2005), Archean cratons and mantle dynamics, *Earth Planet. Sci. Lett.*, *234*, 1–14, doi:10.1016/j.epsl.2005.03.007.
Kirby, S. H. (1983), Rheology of the lithosphere, *Rev. Geophys.*, *21*(6), 1458–1487, doi:10.1029/RG021i006p01458.
Knoll, M., A. Tommasi, R. E. Logé, and J. W. Signorelli (2009), A multiscale approach to model the anisotropic deformation of the lithospheric plates, *Geochem. Geophys. Geosyst.*, *10*, Q08009, doi:10.1029/2009GC002423.
Kogan, L., F. Fisseha, R. Bendick, R. E. Reilinger, S. McClusky, B. King, and T. Soloman (2012), Lithospheric strength and strain localization continental extension from observations of the East African Rift, *J. Geophys. Res.*, *117*, B03402, doi:10.1029/2011JB008516.
Kostrov, V. V. (1974), Seismic moment and energy of earthquakes, and seismic flow of rocks, *Izv. Acad. Sci. USSR Phys. Solid Earth*, *1*, 23–44.
Kreemer, C., W. E. Holt, S. Goes, and R. Govers (2000), Active deformation in eastern Indonesia and the Philippines from GPS and seismicity data, *J. Geophy. Res.*, *105*, 664–680.
Kreemer, C., W. E. Holt, and A. J. Haines (2003), An integrated global model of present-day plate motions and plate boundary deformation, *Geophys. J. Int.*, *154*, 8–34.
Kusznir, N. J., and R. G. Park (1984), Intraplate lithosphere deformation and the strenght of the lithosphere, *Geophys. J. R. Astron. Soc.*, *79*, 513–538.
Lee, C.-T. A., P. Luffi, and E. J. Chin (2011), Building and destroying continental mantle, *Annu. Rev. Earth Planet. Sci.*, *39*, 59–90, doi:10.1146/annurev-earth-040610-133505.
Lindenfield, M., and G. Rümpker (2011), Detection of mantle earthquakes beneath the East African Rift, *Geophys. J. Int.*, *186*, 1–5, doi:10.1111/j.1365-246X.2011.05048.x.
Lister, G. S., M. A. Etheridge, and P. A. Symonds (1986), Detachment faulting and the evolution of pasive contential margins, *Geology*, *14*, 246–250.
Lithgow-Bertelloni, C., and J. H. Guynn (2004), Origin of the lithospheric stress field, *J. Geophys. Res.*, *109*, B01408, doi:10.1029/2003JB002467.
McKenzie, D. (1978), Some remarks on the development of sedimentary basins, *Earth Planet. Sci. Lett.*, *40*, 25–32.
Moucha, R., and A. M. Forte (2011), Changes in African topography driven by mantle convection, *Nat. Geosci.*, *4*, 707–712, doi:10.1038/NGEO1235.
Nyblade, A. A. (2011), The upper mantle low-velocity anomaly beneath Ethiopia, Kenya and Tanzania: Constraints on the origin of the African superswell in eastern Africa and plate versus plume models of mantle dynamics, in *Volcanism and Evolution of the African Lithosphere*, vol. 478, edited by L. Beccaluva, G. Bianchini, and M. Wilson, pp. 37–50, Geol. Soc. of Am., Boulder, Colo.
Nyblade, A. A., H. N. Pollack, D. L. Jones, F. Podmore, and M. Mushayandebvu (1990), Terrestrial heat flow in East and southern African, *J. Geophys. Res.*, *95*(B11), 17,371–17,384.
Pérez-Gussinyé, M., M. M. Metois, M. Fernández, J. Vergés, J. Fullea, and A. R. Lowry (2009), Effective elastic thickness of Africa and its relationship to other proxies for lithospheric structure and surface tectonics, *Earth Planet. Sci. Lett.*, *287*, 152–167, doi:10.1026/j.epsl.2009.08.004.
Priestley, K. D., E. Debayle, and S. Pilidou (2008), The African upper mantle and its relationship to tectonics and surface geology, *Geophys. J. Int.*, *175*, 1108–1126, doi:10.1111/j.1365-246X.2008.03951.x.
Quéré, S., and A. M. Forte (2006), Influence of past and present-day plate motions on spherical models of mantle convection: Implications for mantle plumes and hotspots, *Geophys. J. Int.*, *165*, 1041–1057.
Ranalli, G. (1997), Rheology and deep tectonics, *Ann. Geophys.*, *40*(3), 671–680.
Reilinger, R., et al. (2006), GPS constraints on continental deformation in the Africa-Arabia-Eurasia continental collision zone and implications for the dynamics of plate interactions, *J. Geophys. Res.*, *111*, B05411, doi:10.1029/2005JB004051.
Richardson, R. M., S. C. Soloman, and N. H. Sleep (1979), Tectonic stress in the plates, *Rev. Geophys.*, *17*(5), 981–1019.
Ritsema, J. A., A. A. Nyblade, T. J. Owen, C. A. Langston, and J. C. VanDecar (1998), Upper mantle seismic velocity structure beneath Tanzania, East Africa: Implications for the stability of cratonic lithosphere, *J. Geophys. Res.*, *109*(B9), 21,201–21,213.
Rooney, T., I. D. Bastow, and D. Keir (2011), Insights into extensional processes during magma assisted rifting: Evidence from aligned scoria cones, *J. Volcanol. Geotherm. Res.*, *201*, 83–96, doi:10.1016/j.jvolgeores.2010.07.019.
Rowley, D. B., and D. Sagahain (1986), Depth-dependent stretching: A different approach, *Geology*, *14*(1), 32–35.
Ruppel, C. (1995), Extensional processes in continental lithosphere, *J. Geophys. Res.*, *100*, 24,187–24,215.
Saria, E., E. Calais, Z. Altmamini, P. Pascal, and H. Farah (2013), A new velocity field for Africa from combined GPS and Doris: Contribution to African reference frame, *J. Geophys. Res. Solid Earth*, *118*, 1677–1697, doi:10.1002/jgrb.50137.
Serpelloni, E., G. Vannucci, S. Pondrelli, A. Argani, G. Casula, M. Anzidei, P. Baldi, and P. Gasperini (2007), Kinematics of the Western Africa-Eurasia plate boundary from focal mechanisms and GPS data, *Geophys. J. Int.*, *169*(3), 1180–1200.
Sleep, N. (1990), Hotspots and mantle plumes: Some phenomenology, *J. Geophys. Res.*, *95*(5), 6715–6736.
Stamps, D. S., E. Calais, E. Saria, C. Hartnady, J. M. Nocquet, C. J. Ebinger, and R. M. Fernandes (2008), A kinematic model for the East African Rift, *Geophys. Res. Lett.*, *35*, L05304, doi:10.1029/2007GL03278.
Stamps, D. S., L. M. Flesch, and E. Calais (2010), Lithospheric buoyancy forces in Africa from a thin sheet approach, *Int. J. Earth Sci.*, *99*(7), 1525–1533, doi:10.1007/s00531-010-0533-2.
Steinberger, B., H. Schmeling, and G. Marquart (2001), Large-scale lithospheric stress field and topography induced by global mantle circulation, *Earth Planet. Sci. Lett.*, *186*, 75–91.
Tullis, J. A. (1971), Preferred orientations in experimentally-deformed quartzites, PhD thesis, 362 pp., Univ. of California, Los Angeles, Calif.

Turcotte, D. L., and G. Schubert (2002), *Geodynamics*, 2nd ed., 456 pp., Cambridge Univ. Press, New York.
Venkataraman, A., A. A. Nyblade, and J. Ritsema (2004), Upper mantle Q and thermal structure beneath Tanzania, East Africa from teleseismic *P* wave spectra, *Geophys. Res. Lett.*, *31*, L15611, doi:10.1029/2004GL020351.
Vernant, P., et al. (2004), Present day crustal deformation and plate kinematics in the Middle East constrained by GPS measurements in Iran and Northern Oman, *Geophys. J. Int.*, *157*, 381–398, doi:10.1111/j.1365-246X.2004.02222.x.
Walker, K. T., A. A. Nyblade, S. L. Klemperer, G. H. R. Bokelmann, and T. J. Owens (2004), On the relationship between extension and anisotropy: Constraints from shear wave splitting across the East African Plateau, *J. Geophys. Res.*, *109*, B08302, doi:10.1029/2003JB002866.
Weertman, J., and J. R. Weertman (1975), High temperature creep of rock and mantle viscosity, *Annu. Rev. Earth Planet. Sci.*, *3*, 293–315.
Wernicke, B. (1981), Low-angle normal faults in the Basin and Range Province: Nappe tectonics in an extending orogen, *Nature*, *291*, 645–648, doi:10.1038/291645a0.
Wijk, J. W. V. (2005), Role of weak zone orientation in continental lithosphere extension, *Geophys. Res. Lett.*, *32*, L02303, doi:10.1029/2004GL022192.
Yang, Z., and W.-P. Chen (2010), Earthquakes along the East African Rift System: A multiscale, system wide perspective, *J. Geophys. Res.*, *115*, B12309, doi:10.1029/2009JB006779.
Zhao, D. (2007), Multiscale seismic tomography of mantle plumes and subducting slabs, in *Superplumes: Beyond Plate Tectonics*, edited by D. Zhao, pp. 7–30, Springer, Netherlands.
Zoback, M. L. (1992), First and second-order patterns of stress in the lithosphere: The world stress map project, *J. Geophys. Res.*, *97*(B8), 11,703–11,728.